

Cryo-EM Structures of Respiratory bc1-cbb3 type CIII2CIV Supercomplex and Electronic Communication Between the Complexes

Stefan Steimle

University of Pennsylvania

Trevor Van Eeuwen

University of Pennsylvania <https://orcid.org/0000-0003-0549-1702>

Yavuz Ozturk

University of Pennsylvania

Hee Jong Kim

University of Pennsylvania <https://orcid.org/0000-0002-0823-5301>

Merav Braitbard

Hebrew University

Nur Selamoglu

University of Pennsylvania

Benjamin Garcia

University of Pennsylvania

Dina Schneitman-Duhovny

Hebrew University

Kenji Murakami

UPenn <https://orcid.org/0000-0002-2017-5575>

Fevzi Daldal (✉ fdaldal@sas.upenn.edu)

University of Pennsylvania

Article

Keywords: Cryo-EM Structures, bc1, aa3-type CIV, cyt cy

Posted Date: July 29th, 2020

DOI: <https://doi.org/10.21203/rs.3.rs-48203/v1>

License:   This work is licensed under a Creative Commons Attribution 4.0 International License.

[Read Full License](#)

Version of Record: A version of this preprint was published at Nature Communications on February 10th, 2021. See the published version at <https://doi.org/10.1038/s41467-021-21051-4>.

1 **Cryo-EM Structures of Respiratory *bc₁-cbb₃* type CIII₂CIV Supercomplex and Electronic**
2 **Communication Between the Complexes**

3
4
5
6 Stefan Steimle¹, Trevor VanEeuwen², Yavuz Ozturk^{1, #}, Hee Jong Kim², Merav Braitbard³, Nur
7 Selamoglu¹, Benjamin A. Garcia⁴, Dina Schneidman-Duhovny³, Kenji Murakami^{4,*} and Fevzi
8 Daldal^{1,*}
9

10
11
12
13 ¹Department of Biology, University of Pennsylvania, Philadelphia, PA, 19104; ²Biochemistry and
14 Molecular Biophysics Graduate Group, Perelman School of Medicine, University of Pennsylvania,
15 Philadelphia, PA 19104; [#]Institute of Biochemistry and Molecular Biology, Faculty of Medicine,
16 Albert-Ludwigs University of Freiburg, 79104 Freiburg, Germany; ³School of Computer Science and
17 Engineering, Institute of Life Sciences, The Hebrew University of Jerusalem, Jerusalem, 9190401,
18 Israel and ⁴Department of Biochemistry and Biophysics, Perelman School of Medicine, University
19 of Pennsylvania, Philadelphia, PA 19104
20

21
22
23
24 **Running title:** Bacterial respiratory cytochrome *bc₁-cbb₃* supercomplex
25

26
27
28
29 **Key words:** cytochrome *bc₁* or Complex III; Cytochrome *cbb₃* oxidase or Complex IV; respiratory
30 supercomplex; electron carrier cytochrome *c*; membrane-anchored cytochrome *c_y*; soluble
31 cytochrome *c₂*; *Rhodobacter capsulatus*; respiratory electron transport chain
32

33
34
35
36
37
38
39
40 ***Corresponding authors:** Fevzi Daldal: fdaldal@sas.upenn.edu
41 Phone: +1 215 898-4394
42

43 Kenji Murakami: kenjim@penmedicine.upenn.edu
44 Phone: +1 215 573-1125

45 **Abbreviations**

46 Q, quinone; QH₂, Quinol or hydroquinone; Complex III, CIII₂ or cytochrome *bc*₁, ubiquinol-
47 cytochrome *c* oxidoreductase; Complex IV or CIV, *cbb*₃-type cytochrome *c* oxidase; cyt, cytochrome;
48 cyt *c*₂, cytochrome *c*₂, soluble cytochrome *c*; cyt *c*_y, cytochrome *c*_y, membrane-anchored cytochrome
49 *c*; cyt S-*c*_y, cytochrome *c*_y without its membrane anchor; SC, super-complex; MS, mass spectrometry;
50 XL-MS, cross-linking mass spectrometry; XL, cross-links; TMBZ, 3,3',5,5'-tetramethyl-benzidine;
51 DBH₂, 2,3-dimethoxy-5-methyl-6-*decyl*-1,4-*benzoquinone*; FeS, Rieske iron-sulfur protein; FeS-ED,
52 membrane-extrinsic domain of FeS protein; b position, location of the [2Fe-2S] cluster near heme *b*_L;
53 c position, location of the [2Fe-2S] cluster near heme *c*₁; cryo-EM, cryogenic electron microscopy;
54 BN-PAGE and SDS-PAGE, blue native and sodium dodecylsulfate polyacrylamide gel
55 electrophoresis; C-ter, C-terminus; N-ter, N-terminus; SEC, size exclusion chromatography; TMH,
56 transmembrane helix; DSBU, disuccinimidyl dibutyric urea; DMTMM, 4-(4,6-dimethoxy-1,3,5-
57 triazin-2-yl)-4-methyl-morpholinium chloride; heme-Fe, heme-iron; E_m, redox midpoint potential;
58 heme *c*_{p1}, N-ter *c*-type heme 1 of CcoP; heme *c*_{p2}, C-ter *c*-type heme 2 of CcoP; heme *c*_o, *c*-type heme
59 of CcoO; RMSD, root-mean-square deviation; DDM, n-dodecyl β-D-maltoside.

60 **Abstract**

61 Respiratory electron transport complexes are organized as individual entities or combined as large
62 super-complexes (SC). The Gram-negative bacteria deploy a mitochondrial-like cytochrome (cyt)
63 bc_1 (Complex III, CIII₂), and may have specific cbb_3 -type cyt c oxidases (Complex IV, CIV) instead
64 of the canonical aa_3 -type CIV. Electron transfer between these complexes is mediated by soluble (c_2)
65 and membrane-anchored (c_y) cyts. Here, we report the first structure of a bc_1 - cbb_3 type SC (CIII₂CIV,
66 5.2Å resolution) and three conformers of native CIII₂ (3.3Å resolution) of functional relevance. The
67 SC contains all catalytic subunits and cofactors as well as two extra transmembrane helices attributed
68 to cyt c_y and the assembly factor CcoH. The cyt c_y is integral to SC, its cyt domain is mobile and
69 conveys electrons to CIV differently than cyt c_2 . For the first time, this work establishes the structural
70 characteristics of membrane-confined and membrane-external electron transport pathways of SCs in
71 Gram-negative bacteria.

72 **Introduction**

73 Respiratory chains couple exergonic electron transport from nutrients to the terminal acceptor oxygen
74 (O_2), and generate a proton motive force used for ATP synthesis. Complex I (NADH dehydrogenase)
75 and Complex II (succinate dehydrogenase) are the entry points into the chain of reducing equivalents,
76 and reduce quinone (Q) to hydroquinone (QH_2). Complex III (cytochrome (cyt) bc_1 or $CIII_2$) oxidizes
77 QH_2 to reduce cyt c , which is then oxidized by Complex IV (cyt c oxidase or CIV) converting oxygen
78 to water ¹ (**Fig. 1A**).

79 Respiratory complexes are evolutionarily conserved, but bacterial enzymes are structurally
80 simpler, consisting mainly of the catalytic subunits. $CIII_2$ is a dimer with each monomer comprised
81 of three subunits: the Rieske FeS (FeS) protein with a [2Fe-2S] cluster, cyt b with hemes b_H and b_L ,
82 and cyt c_1 with heme c_1 cofactors (**Fig. 1A,B**). The FeS protein external domain (FeS-ED) is mobile
83 between the **b** (close to heme b_L) and **c** (close to heme c_1) positions ^{2,3}. Some bacterial species such as
84 *Rhodobacter capsulatus* ⁴ and pathogens like *Helicobacter pylori*, *Campylobacter jejuni* ⁵ and
85 *Neisseria* ⁶ contain only a high oxygen affinity cbb_3 -type CIV to support their micro-aerophilic
86 growth. The cbb_3 -type CIV is a monomer comprised of four subunits: CcoN with heme b and heme
87 b_3 -Cu binuclear center, CcoO with heme c_o , CcoQ, and CcoP with hemes c_{p1} and c_{p2} cofactors ⁷ (**Fig.**
88 **1A,B**).

89 Many Gram-negative bacteria contain both soluble and membrane-anchored (via transmembrane
90 domains or fatty acids) cyts c as electron carriers (*e.g.*, *Rhodobacter capsulatus* cyt c_y ⁸, *Paracoccus*
91 *denitrificans* cyt c_{552} ⁹, and *Helicobacterium gestii* cyt c_{553} ¹⁰). Conversely, Gram-positive bacteria
92 have no freely diffusing electron carrier, but contain cyt c domains fused to their $CIII_2$ such as in
93 *Mycobacterium smegmatis* ¹¹, or CIV such as in *Bacillus subtilis* ¹². In *R. capsulatus*, both the
94 diffusible cyt c_2 and the membrane-anchored cyt c_y are electron carriers from $CIII_2$ to CIV in
95 respiration ¹³.

96 In recent years, the co-occurrence of individual complexes together with multi-enzyme super-
97 complexes (SCs) in energy-transducing membranes has become evident ^{14,15}. However, the role of
98 this heterogeneity is debated ^{16,17}. SCs may enhance catalytic efficiency through substrate/product
99 channeling, or minimize production of harmful reactive oxygen species to decrease cellular distress
100 ¹⁸. The structures of mitochondrial SCs, such as CIII₂CIV or its smaller variants CIII₂ and
101 CIII₂CIV ¹⁹ are well-known ^{20,21}. Some bacterial SCs (*e.g.*, *P. denitrificans* ²² or *C. glutamicum* ²³)
102 have also been characterized biochemically, but only the structure of the Gram-positive *M. smegmatis*
103 SC (CIII₂CIV₂) is known ^{24,25}.

104 As of yet, no respiratory SC structure has been determined for Gram-negative bacteria, the
105 evolutionary precursors of mitochondria. Moreover, SCs containing *cbb*₃-type ancient forms of CIV
106 with primordial respiratory features remain unknown ²⁶. Such structural studies have been hampered
107 due to unstable interactions between CIII₂ and CIV, hence their trace amounts in nature. We have
108 overcome this hurdle using a genetic approach, yielding large amounts of SCs from the Gram-
109 negative facultative phototroph *R. capsulatus*. Here, we report the first cryo-EM structure of a *bc*₁-
110 *cbb*₃ type SC (CIII₂CIV, at 5.2Å resolution), as well as three structural conformers of native CIII₂ (at
111 3.3-4.2Å resolution). Moreover, we show that the membrane-bound cyt *c*_γ and the diffusible cyt *c*₂
112 interact differently with CIV for electron transfer. For the first time, this work establishes the
113 structural features of CIII₂CIV and its distinct respiratory electron transport pathways (membrane-
114 confined and membrane-peripheral) in Gram-negative bacteria.

115 **Results**

116 **Isolation, and characterization of functional fused SCs.** Earlier studies have indicated that in *R.*
117 *capsulatus* CIII₂, CIV, and cyt *c_y* are in close proximity to each other²⁷. Analyses of membranes from
118 this species indicated barely detectable entities around ~450 kDa M_r, larger than the masses of CIV
119 monomers or CIII₂ dimers (**Fig. S1A,B**). However, these entities were of low abundance and highly
120 unstable, rendering their study difficult.

121 During the assembly processes of CIII₂ and CIV, cyt *c₁* interacts with cyt *b* to form a cyt *b-c₁*
122 subcomplex²⁸, and CcoP associates with CcoNOQ subcomplex to yield an active CIV²⁹. We surmised
123 that translationally fusing the C-terminus (C-ter) of cyt *c₁* to the N-terminus (N-ter) of CcoP (on the
124 inner (*n*) side of the membrane) as a cyt *c₁*-CcoP fusion might produce a stable bipartite *bc₁-cbb₃* type
125 SC (left panels of **Fig. 1C,D**). Also, adding the 69-residue linker (L) and the 100-residue cyt domain
126 of *c_y* to the C-ter of cyt *c₁*-CcoP (on the outer (*p*) side of the membrane) as a cyt *c₁*-CcoP-*c_y* protein
127 might yield a tripartite SC with its attached electron carrier (right panels of **Fig. 1C,D**). This approach
128 (Supplemental Information, Methods) was successful, and yielded constructs (**Fig. S1B** and **Table**
129 **S1**) that complemented a mutant lacking CIII₂ and CIV for photosynthesis-proficiency (*i.e.*, CIII₂
130 activity) and CIV activity (**Fig. S1C**).

131 The His-tagged bipartite and Flag-tagged tripartite SCs were purified by tag-affinity and size
132 exclusion chromatography (SEC) (SI, Methods) (**Fig. S1D,E**). Analyses of isolated proteins showed
133 that they contained large entities of M_r ~450 kDa range (**Fig. S1D,E** fractions A-1 and B-1 in insets)
134 that had the cyt *c₁*-CcoP (~65 kDa) or cyt *c₁*-CcoP-*c_y* fusions (~80 kDa) (**Fig. S1F**), and all protein
135 bands were identified by mass spectrometry (MS) as the subunits of CIII₂ and CIV (**Table S2**). The
136 fusion proteins contained covalently-attached heme cofactor(s) as revealed by a *c*-type cyt specific
137 staining (**Fig. S1G**). CcoQ (M_r ~7kDa) of CIV was absent in both SC preparations.

138 Purified SCs were characterized for their cyts *b* and *c* contents. The optical redox difference
139 spectra were distinct from those of CIII₂³⁰ or CIV³¹, and the tripartite SC contained more *c*-type cyt
140 than the bipartite SC, due to the additional cyt domain of *c_y* (**Fig. S1H**). Both SC preparations were
141 active, exhibiting QH₂:cyt *c* reductase (specific to CIII₂) and cyt *c* reductase (specific to CIV)
142 activities (**Fig. S1I,J**). Moreover, the tripartite SC also had QH₂:O₂ reductase (coupled CIII₂+CIV)
143 activity without addition of horse heart cyt *c* or *R. capsulatus* cyt *c*₂ (**Fig. S1K**). Thus, the cyt domain
144 of *c_y* fused to cyt *c*₁-CcoP transferred electrons from CIII₂ to CIV.

145

146 **Structures of the tripartite SCs.** Cryo-EM analysis of the tripartite SC preparations (**Fig. S1E**,
147 fraction B-1) showed that the initial 3D classes were mainly of two different sizes (**Fig. S2**, Box 1,
148 left). The size (~180Å length) and shape of the smaller particles suggested that these may correspond
149 to a dimeric CIII₂ associated with a single CIV. Focused classification and processing of the subclass
150 containing ~62,000 particles with the highest initial resolution and best discernable features, led to a
151 tripartite CIII₂CIV map (SC-1A, EMD-22228) at 6.1Å resolution (**Fig. S2A**, SI Methods), while
152 another dataset yielded a lower resolution map (SC-1B, EMD-22230) at 7.2Å (**Fig. S2B**) (**Table S3**).
153 The larger particles (~250Å length, **Fig. S2**, Box 1, left) represented a dimeric CIII₂ flanked by two
154 CIV, as expected based on two *c*₁-CcoP-*c_y* subunits *per* CIII₂. However these particles were rare
155 (~5,000) and their map (SC-1C) could not be refined beyond ~10Å resolution (**Fig. S2C**).

156 A homology model of *R. capsulatus cbb*₃-type CIV was built using the highly homologous *P.*
157 *stutzeri* structure (PDB: 3MK7; 3.2Å resolution) as a template (SI, Methods, **Table S3**). The available
158 CIII₂ model (PDB: 1ZRT; 3.5Å resolution) was further refined (PDB: 6XI0; 3.3Å resolution) using
159 our cryo-EM data (**Table S3**). These models were fitted as rigid bodies into the maps SC1-A and SC-
160 1B (**Fig. S3A**), with correlation coefficients CC_{box} of 0.75 and CC_{box} of 0.71, respectively (**Table S3**).
161 The [2Fe-2S] clusters of the FeS proteins of CIII₂ could be recognized closer to b (heme *b_L*) than to c

162 (heme c_1) positions, but had lower occupancy and resolution likely due to conformational
163 heterogeneity. The heterogeneity of the FeS-ED of CIII₂ in monomer B (away from CIV) was more
164 pronounced than that in monomer A (adjacent to CIV) (**Fig. S3B**). Lower resolutions of the CIII₂ FeS-
165 ED portions were anticipated due to their mobility ^{2,3}.

166 Superimposition of the CIII₂ portions of SC-1A and SC-1B maps showed that CIV was in different
167 orientations in different maps (**Fig. S3C**). The two extreme locations of CIV with respect to CIII₂
168 were displaced from each other by a translation of $\sim 3\text{\AA}$ and a rotation of ~ 37 degrees (**Fig. S3D, E**;
169 SC-1A in red, and SC-1B in blue). Other subclasses identified in 3D classifications showed CIV in
170 various orientations between those seen in SC-1A and SC-2B maps. This CIII₂CIV interface
171 flexibility is attributed to the limited interaction between the CcoP (N-ter TMH) of CIV and the cyt
172 *b* (TMH7) of CIII₂ (**Fig. 2**, top view). In the interface regions of SC-1A and SC-1B maps, additional
173 weaker features that are not readily attributable to CIII₂ and CIV structures were also observed.
174 However, no membrane-external feature that might correspond to cyt domain of c_y , which is an
175 integral part of the cyt c_1 -CcoP- c_y subunit, could be discerned in these maps.

176
177 **Structure of bipartite SC supplemented with cyt c_y .** The bipartite SC preparations (**Fig. S1D**,
178 fraction A-1) were supplemented with either purified full-length cyt c_y , or its soluble variant lacking
179 the TMH (*i.e.*, cyt S- c_y) ³², to yield the bipartite SC+ c_y and SC+S- c_y samples. Following SEC, the
180 elution fractions showed that only the intact cyt c_y , but not the cyt S- c_y , remained associated with the
181 SC (**Fig. S4A**). Thus, the cyt c domain of c_y does not bind tightly to, and its TMH is required for
182 association with, the SC.

183 The cryo-EM analyses of the bipartite SC+ c_y yielded a map (SC-2A, EMD-22227) at 5.2 \AA
184 resolution (**Fig. S5A,B**), with local resolutions ranging from 4.3-8.0 \AA (**Fig. S6A,C**). The homology
185 model of CIV and the refined model of CIII₂ (PDB: 6XI0) were fitted as rigid bodies into SC-2A

186 (**Fig. 2A**), with a correlation coefficient CC_{box} of 0.74 (**Table S3**). Comparison of SC-2A (bipartite
187 CIII₂CIV) with SC-1A (tripartite CIII₂CIV) showed that these maps were highly similar, with RMSD
188 of 1.6 Å. Hence, they are collectively referred to as CIII₂CIV, irrespective of their bipartite or tripartite
189 origins.

190 The dimensions (~155x60x90Å, LxWxH) of the slightly curved CIII₂CIV structure were
191 consistent with a CIII₂ dimer associated with one CIV. On SC-2A map at 5.2Å resolution, some large
192 aromatic side chains could be readily discerned (**Fig. 2B**). Of the TMHs seen, 34 were accounted for
193 by two FeS proteins, two cyts *b* and two cyts *c*₁ (2, 16 and 2 TMHs per dimer, respectively), and
194 single CcoN, CcoO and CcoP (12, 1 and 1 TMHs, respectively) (**Fig. 2C**). The features corresponding
195 to the heme cofactors of CIII₂CIV were attributed to hemes *b*_H and *b*_L of cyt *b*, heme *c*₁ of cyt *c*₁, and
196 to hemes *b* and *b*₃ of CcoN, heme *c*_o of CcoO and hemes *c*_{p1} and *c*_{p2} of CcoP proteins. Like the tripartite
197 maps, the [2Fe-2S] clusters of CIII₂ had lower resolution and were located closer to heme *b*_L (b
198 position). An additional TMH was observed at the distal end of CIV (**Fig. 2A**, rotated 180 degrees in
199 **Fig. 2D**) close to CcoN TMH3 and TMH4 (**Fig. 2C**). Due to its location, this TMH (depicted in **Fig.**
200 **2** as an *ab initio* model of CcoN Arg25-Leu48 residues) was tentatively attributed to the extra N-ter
201 TMH (*i.e.*, TMH0) of CcoN, specific to *R. capsulatus*.

202 The interface of CIII₂CIV is delimited by CcoN TMH8 and TMH9, CcoP TMH, cyt *b* TMH5 and
203 TMH7, and cyt *c*₁ TMH of monomer A, with the closest interaction being between CcoP TMH and
204 cyt *b* TMH7 (**Fig. 2A,C**). Two interacting TMHs of unknown identities (**Fig. 2D**, in red and blue),
205 and an inter-complex connection are seen at the interface. This connection is at the *n* face of the
206 membrane, near the TMHs of cyt *c*₁ and CcoP (**Fig. 2E**, Lys257_{c1} and Thr13_{CcoP}), and tentatively
207 attributed to their covalent junction, linking CIII₂ to CIV.

208

209 **The assembly factor CcoH and cyt c_y TMHs are located at CIII₂CIV interface.** A co-evolution
210 based approach predicting the residue-residue contacts in protein-protein interactions, RaptorX-
211 ComplexContact³³, was used to identify the TMHs at the CIII₂CIV interface. The single TMH
212 containing CIV-related proteins (*i.e.*, CcoQ subunit, CcoS and CcoH assembly factors²⁹ and cyt c_y ⁸)
213 were analyzed against the subunits of CIII₂ and CIV. Significant predictions of interacting residue
214 pairs (confidence value >0.5) were found only between CcoN (primarily TMH9) and the putative N-
215 term TMH of CcoH (**Fig. S7A,B**). An *ab initio* model of CcoH TMH was docked via PatchDock³⁴
216 onto CIV using the predicted residue-residue contacts as distance restraints (15 Å threshold) (SI,
217 Methods). The top scoring models converged to a single cluster at the location of the unknown TMH,
218 next to CcoN TMH9 (**Fig. S7C**). Examination of the interactions between CcoH TMH and CcoN
219 TMH9 showed multiple co-evolutionarily conserved residues in close contacts (**Fig. S7B,D**). Earlier
220 studies had indicated that CcoH can be cross-linked by disuccinimidyl suberate (spacer length ~11Å)
221 to CcoP and CcoN³⁵. Thus, the TMH close to CcoN TMH9 (**Fig. 2E**, blue TMH) was tentatively
222 assigned to the assembly factor CcoH.

223 An important difference between the maps SC-2A (bipartite CIII₂CIV+ c_y) and SC-1A (tripartite
224 CIII₂CIV) was seen at the interface. The unidentified TMHs were barely visible in SC-1A, but highly
225 enhanced in SC-2A (**Fig. 2E**), indicating higher occupancy. The observation that only the native cyt
226 c_y binds to bipartite SC via its TMH suggested that the TMH (red in **Fig. 2E**) next to CcoH TMH
227 (blue in **Fig. 2E**) may correspond to the membrane-anchor of cyt c_y . This explanation is supported by
228 fact that the bipartite CIII₂CIV+ c_y was supplemented with full-length cyt c_y while the tripartite SC
229 contained only the fused cyt domain of c_y . Indeed, landmark densities corresponding to the helix-
230 breaking Gly11 and the correctly spaced bulky side chains of Phe15 and Tyr21 of cyt c_y TMH (NH₂-
231 xxx**Gly11**xxx**Phe15**xxxxx**Tyr21**-COOH) were discerned (**Fig. 2F**).

232 We noted that some CIII₂CIV+c_y subclasses exhibited a weak feature on the *p* side of the
233 membrane that may reflect the cyt domain of c_y (**Fig. S5G, SC-2B**). However, this feature could not
234 be refined to high resolution, consistent with the weak binding of cyt domain of c_y to CIII₂CIV.
235 Moreover, the predominant conformation of CIV in the bipartite CIII₂CIV+c_y (**Fig. S5A,B, SC-2A**)
236 shifted towards that seen in map SC-1A of tripartite SC (**Fig. S2A**), with no major class corresponding
237 to SC-1B (**Fig. S2B**). This suggested that local interactions between the CcoH and cyt c_y TMHs and
238 CIV decreased the interface flexibility of CIII₂CIV (**Fig. 2E**).

239

240 **Cryo-EM structures of *R. capsulatus* native CIII₂.** The bipartite SC+c_y samples contained large
241 amounts of smaller particles (~110Å length) (**Fig. S2, Box 2**) that were the size of CIII₂ (**Fig. S5C,D**).
242 Analyses of these particles using C2 symmetry led to the map CIII₂ at 3.3Å resolution for native CIII₂
243 (**Fig. S5E**), with local resolutions ranging from 3.0 to 4.0Å (**Fig. S6B,D**) (**Table S3**). The FeS-ED
244 parts showed lower occupancy and resolution compared to the rest of the map, indicating
245 conformational heterogeneity. When similar analyses were carried out without imposing C2
246 symmetry, three distinct maps were obtained for CIII₂ (CIII₂ c-c, CIII₂ b-c and CIII₂ b-b at 3.8, 4.2
247 and 3.5Å resolutions, respectively) (**Fig. S5F**). These maps were superimposable with respect to cyt
248 *b* and cyt c₁ subunits, except for the FeS-ED portions. The CIII₂ structures depicted by the CIII₂ b-b
249 (**Fig. 3A-C**) and CIII₂ c-c (**Fig. 3D**) maps exhibited overall C2 symmetry, but in the former the FeS-
250 EDs were located in b, whereas in the latter in c position³. Notably, the third structure (CIII₂ b-c) was
251 asymmetric, with the FeS-ED of one monomer being in c, and the other one in b positions (**Fig. 3E**).
252 Such asymmetric structures of native CIII₂ have not been observed frequently, although they are
253 proposed to occur during QH₂ oxidation³⁶⁻³⁸.

254

255 **Interactions of cyt c_2 and cyt c_y with CIII₂CIV.** The interaction interfaces between CIII₂CIV and
256 its physiological electron carriers were analyzed by cross-linking mass spectrometry (XL-MS) ^{39,40}.
257 The co-crystal structure (PDB: 3CX5) of yeast CIII₂ with its electron carrier iso-1 cyt c ⁴¹ was used
258 as a template (homology between yeast cyt c_1 and *R. capsulatus* cyt c_1 : 31% identity and 58%
259 similarity; iso-cyt c and cyt c_2 : 25% identity and 56% similarity) to model the binding of cyt c_2 on
260 bacterial CIII₂. The *R. capsulatus* cyt c_1 (PDB: 6XI0) and cyt c_2 (PDB: 1C2N) structures were
261 superimposed with their yeast counterparts on the co-crystal structure, and a model with a single cyt
262 c_2 docked to a monomer of CIII₂ was obtained (**Fig. S4C**). To experimentally verify this model, the
263 protein cross-linker 4-(4,6-dimethoxy-1,3,5-triazin-2-yl)-4-methyl-morpholinium chloride
264 (DMTMM) was used (SI, Methods). The intra-subunit cross-links (XLs) within CIII₂CIV provided
265 controls, and high-confidence XLs were identified using both FindXL ⁴² and MeroX ⁴³ search engines
266 (**Table S4**). The three XLs between cyt c_1 and cyt c_2 provided distance restraints ($\sim 30\text{\AA}$ for DMTMM)
267 for docking cyt c_2 to CIII₂ (**Table S4**) (**Fig. S4D**), and the docking models clustered at a single region
268 per monomer of CIII₂ (**Fig. 4A**, right). This region overlapped with the binding site of cyt c_2 defined
269 by the model obtained by alignment to the yeast co-crystal structure (**Fig. S4E**). The distance from
270 cyt c_2 heme-Fe to cyt c_1 heme-Fe was $\sim 16.8\text{\AA}$ for the co-crystal derived model, while comparable
271 distances were between $\sim 13.8 - 20.4\text{\AA}$ with the docking models. Thus, docking via Patchdock
272 integrating XL-MS mediated distance restraints defined reliably, but with limited accuracy, the
273 interaction region of cyt c_2 on CIII₂.

274 No information about the binding of cyt c_2 and *cbb*₃-type CIV was available. This binding was
275 first shown biochemically (**Fig. S4B**), and then subjected to the XL-MS with DMTMM approach.
276 The XLs between the proteins (1 between cyt c_2 and CcoP, and 8 between cyt c_2 and CcoO) provided
277 distance restraints for docking cyt c_2 to CIV (**Table S4**). The docking models clustered in a single
278 region of CIV (**Fig. 4A**, left), closer to heme c_{p2} (c_2 heme-Fe to c_{p2} heme-Fe: ~ 15.2 to 35.6\AA) than

279 heme c_{p1} (c_2 heme-Fe to c_{p1} heme-Fe: ~ 23.0 to 42.0\AA) of CcoP subunit (**Fig. 5**). The two cyt c_2 binding
280 regions on CIII₂CIV are highly distant from each other (closest c_2 heme-Fe on CIII₂ to that on CIV is
281 $\sim 69\text{\AA}$) (**Fig. 5A**).

282 Next, the binding interactions between cyt domain of c_y and CIII₂CIV were sought using
283 DMTMM and disuccinimidyl dibutyric urea (DSBU) as cross-linkers. Similar to DMTMM, DSBU
284 yielded multiple intra-subunit XLs within the subunits of CIII₂CIV as experimental controls (**Table**
285 **S4**). Six XLs (five cyt c_y to cyt c_1 and one cyt c_y to FeS protein) were found with DMTMM, four XLs
286 (only cyt c_y to FeS protein) with DSBU (**Table S4**), and none were observed between cyt c_y and CIV,
287 suggesting that cyt domain of c_y is closer to CIII₂ in CIII₂CIV. In this case, PatchDock generated two
288 binding clusters for cyt domain of c_y on each CIII₂ monomer of SC. One of the clusters was on cyt c_1
289 and overlapped with cyt c_2 cluster (**Fig. 4B**), whereas the other one was between cyt c_1 and the FeS-
290 ED near CIII₂ inter-monomer space (**Fig. S4F-H**). The two clusters 1 and 2 are best visible in a top
291 view (**Fig. S4H**), and the distances between cyt c_y heme-Fe and cyt c_1 heme-Fe of CIII₂ monomer A
292 are between 13.8 to 47.1\AA (**Fig. 5**). To further support these binding locations, we searched in our
293 cryo-EM datasets 3D classes that contained extra features corresponding to cyt domain of c_y . A minor
294 class ($\sim 18,000$ particles) (**Fig. S5G**) showing an extra feature attributable to cyt domain of c_y between
295 CIV and CIII was found (**Fig. S4F,G**).

296 Similar dockings of cyt domain of c_y were repeated using the different conformers of native CIII₂
297 (**Fig. 3C-E**, CIII₂ b-b, c-c and b-c). When the FeS-EDs are in c position (CIII₂ c-c), the docking
298 models gathered as a single cluster on cyt c_1 , slightly displaced towards the FeS-ED of the same
299 monomer (**Fig. S8A-C**). However, when the FeS-EDs are in b position (CIII₂ b-b), such models were
300 more spread out (**Fig. S8D-F**). The third model with one FeS-ED in c and the other in b positions
301 yielded the expected clustering pattern depending on the local FeS-ED conformation. In CIII₂CIV
302 both FeS-EDs being in the b position, we assumed that cyt domain of c_y docks similarly to that seen

303 with CIII₂ b-b, and that the spreading of docking is due to the variable conformations of the FeS-EDs
304 in SC (**Fig. S8**). In addition, since heme *c*₁ and not the FeS protein is the electron exit site of CIII₂
305 ^{44,45}, we imply that the cluster on cyt *c*₁ is the productive binding region of cyt domain of *c*_y.

306 Examination of all pertinent distances between the cofactors of CIII₂CIV (**Fig. 5A**) indicates that
307 the binding region of cyt domain of *c*_y near heme *c*₁ is far from CIV. The large distance (~50.8Å)
308 separating cyt *c*₁ heme-Fe of CIII₂ monomer A from CcoP *c*_{p1} heme-Fe (the closest compared with
309 heme *c*_{p2}) makes it impossible to define a position for cyt *c*_y close enough to heme *c*₁ reducing it, and
310 heme *c*_{p1} oxidizing it, while transferring electrons from CIII₂ to CIV. The distance constraint, the
311 inability to resolve the cyt domain of cyt *c*_y by cryo-EM, and the frequent XLs to CIII₂ led us to
312 conclude that cyt *c*_y must oscillate within CIII₂CIV during QH₂:O₂ oxidoreduction (**Fig. 6**).

313 **Discussion**

314 Prior to this work, no structural information was available on any *cbb*₃-type CIV containing SC, or
315 its interactions with its physiological electron carriers. Here, we describe the first cryo-EM structures
316 of CIII₂CIV, a *bc*₁-*cbb*₃ type respiratory SC from the Gram-negative, facultative phototroph *R.*
317 *capsulatus*. We define the likely binding regions of cyt *c*₂ and cyt *c*₃ to CIII₂CIV, and also report three
318 structural conformers of native CIII₂ at high resolution. Although 3D structures of bacterial *bc*₁-type
319 CIII₂ are available, native CIII₂ heterodimers have not been reported. Similarly, only one structure
320 was available for *cbb*₃-type CIV⁴⁶. Members of this subfamily of heme-Cu:O₂ reductases are
321 widespread among bacteria and essential for microaerobic processes, including anaerobic
322 photosynthesis and bacterial infection⁴. Unlike the obligate CIII₂CIV₂ SC of *Actinobacteria*, which
323 is rigid^{24,25}, the facultative CIII₂CIV of *R. capsulatus* is naturally flexible, limiting its structural
324 resolution. In such species, the dual function of CIII₂, interacting with the photochemical reaction
325 center and CIV, may require this natural flexibility to allow swift metabolic adaptations.

326 Isolation of CIII₂CIV was only possible using a genetically modified strain carrying a translational
327 fusion between CIII₂ and CIV (SI, Methods). The fusion approach yielded compositionally
328 heterogeneous preparations, containing mixtures of CIII₂CIV₂, CIII₂CIV and CIII₂ particles, possibly
329 due to subunit sub-stoichiometry, incomplete assembly, or high susceptibility to degradation.
330 Insertion of different spacers at the cyt *c*₁-CcoP fusion junction, overexpression of the subunits and
331 related assembly components could not overcome this heterogeneity (SI, Methods). Consequently,
332 structural studies required extensive data collections, limited structural resolution, but allowed
333 analyses of fragmented particles.

334 **Structures of CIII₂CIV.** The structures of the tripartite CIII₂CIV or bipartite CIII₂CIV+*c*₃ were
335 highly similar at sub-nanometer resolution (~5.2 to 7.2Å). Their flexibility was due to limited protein-
336 protein interactions at their interface, where the TMHs of cyt *c*₃ and CcoH are located (**Fig. 2**).

337 Previously, neither the exact location nor the mobility of cyt c_y between CIII₂ and CIV were known.
338 The SC structure shows that the N-terminal TMH of cyt c_y is locked at the interface, allowing mobility
339 of its cyt domain within CIII₂CIV (**Fig. 6**). Although the linker region of cyt c_y remains unresolved,
340 it is long enough to reach both CIII₂ and CIV. Earlier studies with *R. capsulatus* cyt c_y had shown that
341 a full-length linker (69 residues) is needed for rapid (< ~50 μsec) electron transfer from CIII₂ to the
342 photosynthetic reaction center ⁴⁷ whereas a shorter linker (~45-residues) is fully proficient for
343 respiratory electron transfer to CIV⁴⁸.

344 **Structures of bacterial native CIII₂.** In native CIII₂ conformers, different positions of the [2Fe-2S]
345 cluster bearing FeS-EDs were observed. Crystallographic structures have often depicted bacterial
346 CIII₂ as symmetrical homodimers ^{3,49,50}. These structures were obtained in the presence of inhibitors
347 constraining FeS-EDs near heme b_L or used mutants stabilizing it on cyt b surface. Alternatively, they
348 contained crystal contacts restricting the FeS-ED movement ⁵¹. To our knowledge, no native
349 heterodimeric CIII₂ structure of bacterial origin with different conformations of its FeS-EDs has been
350 reported. Only recent cryo-EM structures of mitochondrial SCs have shown different maps for CIII₂
351 FeS-EDs ^{17,52}. Thus, native CIII₂ is not always a symmetric homodimer, and the FeS-ED of each
352 monomer is free to move independently from the other. The Q-cycle models describe the mechanism
353 of CIII₂ catalysis by two turnovers of a given monomer, with the different positions of the FeS-ED
354 protein attributed to different catalytic steps ^{3,44,45}. Emerging asymmetric structures of bacterial and
355 mitochondrial native CIII₂ obtained by cryo-EM in the absence of inhibitors or mutations, combined
356 with the inter-monomer electron transfer between the hemes b_L of the monomers ^{53,54}, provide a
357 glimpse into plausible “heterodimeric Q cycle” mechanism(s) ^{37,38}. Accordingly, the FeS-EDs of CIII₂
358 monomers might cycle between homo- and hetero-dimeric conformations during the Q-cycle.

359 **Electronic communication between CIII₂CIV partners.** This work defined hitherto unknown
360 structural interactions between the cyt c_2 or cyt c_y and CIII₂CIV (**Fig. 6**). The CIII₂CIV structure

361 indicates that the distances separating heme c_1 of CIII₂ monomer A and hemes c_{p1} or c_{p2} of CIV are
362 too large (**Fig. 5**) for direct microsecond scale electronic communication⁵⁵ to sustain the turnover rate
363 of CIII₂CIV. Even when CIII₂ and CIV form a SC, an electron carrier is still required for QH₂:O₂
364 oxidoreduction. The binding location of cyt c_2 on CIV defined here, the redox midpoint potentials
365 (E_m) of the cofactors, and the distances separating them (**Fig. 5A**) suggest that cyt c_2 would confer
366 electrons to the closer heme c_{p2} , rather than the more distant heme c_{p1} , of CcoP. This will then initiate
367 canonical electron transfer via heme c_{p1} , heme c_o and heme b to heme b_3 -Cu_B site for O₂ reduction^{56,57}
368 (**Fig. 6**). For purified *R. capsulatus* proteins, the E_m values of cyt c_2 , cyt c_1 ³⁰ and heme c_o of CcoO are
369 known³¹. The E_m values of *R. capsulatus* CcoP hemes c_{p1} and c_{p2} are unknown, but based on similar
370 E_m values of heme c_o for *B. japonicum* and *R. capsulatus*, they are expected to be similar⁵⁸.

371 The likely interaction region of cyt c_y on cyt c_1 of CIII₂, which is close to that of cyt c_2 is now
372 known, but that on CIV remains less well defined. The distance separating the redox centers is a major
373 factor that controls the rate of electron transfer⁵⁵. The binding region of cyt domain of c_y on CIII₂
374 suggests that reduced cyt c_y , upon its movement to CIV, might preferentially convey electrons to the
375 closer heme c_{p1} than heme c_{p2} of CcoP (**Fig. 6**). If so, under physiological conditions, heme c_{p1} would
376 be the primary receiver of electrons derived from QH₂ oxidation by CIII₂, forming a fully membrane-
377 confined electronic wiring within CIII₂CIV. In contrast, cyt c_2 carries electrons from heme c_1 to heme
378 c_{p2} via free diffusion. This membrane-external pathway might accommodate electrons not only from
379 QH₂ but also from other donors distinct from CIII₂. As such, reduction of cyt c_2 during methylamine
380 oxidation⁵⁹, or degradation of sulfur containing amino acids, converting toxic sulfite (SO₃²⁻) to sulfate
381 (SO₄²⁻) by sulfate oxidase⁶⁰ might provide electrons to CIV, contributing to cellular energy
382 production.

383 In summary, the architecture of CIII₂CIV along with its dynamics and interactions with its
384 physiological redox partners established salient structural features of two distinct respiratory electron

385 transport pathways (membrane-confined and membrane-external) that operate between CIII₂ and CIV
386 in Gram-negative bacteria for the first time.

387 **Acknowledgments**

388 This work was supported partly by the NIH grants, GM 38237 to FD, GM123233 to KM, GM110174
389 and AI118891 to BAG, T32-GM008275 to TV, T32-GM071339 to HJK, and partly by the Division
390 of Chemical Sciences, Geosciences and Biosciences, Office of Basic Energy Sciences of Department
391 of Energy grant DE-FG02-91ER20052 to FD, by ISF 1466/18, BSF 2016070, and Ministry of Science
392 and technology 80802 grants to DS. YO was supported by the grant GRK2202-23577276/RTG from
393 DFG, Germany. Data analysis was partly supported by the NIH grant S10OD023592.

394 We thank Drs. S. Saif Hasan, Brian G. Pierce and Christian Presley at the Institute for Bioscience
395 and Biotechnology Research, University of Maryland, for insightful discussions and invaluable help
396 they provided during this study. SS and FD thank Vivian Kitainda for her assistance with protein
397 purification and O₂ consumption measurements.

398 This research was supported in part by the NCI, National Cryo-EM Facility at the Frederick
399 National Laboratory for Cancer Research under contract HSSN261200800001E. The authors thank
400 Ulrich Baxa, Thomas Edwards and Adam Wier for their support and helpful discussions. Some cryo-
401 EM data were also obtained at the University of Massachusetts Cryo-EM Core Facility, and we thank
402 Drs. Chen Xu, KangKang Song and Kyoungwan Lee for their support. Cryo-EM sample screening
403 and optimization was performed at the Electron Microscopy Resource Laboratory at the Perelman
404 School of Medicine, University of Pennsylvania, and we thank Dr. Sudheer Molugu for his support.

405 **Data deposition**

406 The following *R. capsulatus* structures and the corresponding cryo-EM maps are deposited to PDB
407 and EMDB: CIII₂ (PDB: 6XI0; EMD-22189); CIII₂ c-c (PDB: 6XKT; EMD-22224); CIII₂ b-c (PDB:
408 6XKU; EMD-22225); CIII₂ b-b (PDB: 6XKV; EMD-22226); SC-2A (PDB: 6XKW; EMD-22227);
409 SC-1A (PDB: 6XKX; EMD-22228) and SC-1B (PDB: 6XKZ; EMD-22230). The raw XL-MS data
410 deposited to PRIDE repository (<http://www.ebi.ac.uk/pride/archive/>) with the dataset identifier
411 PXD020038.

412

413 **Authors Contributions**

414 All authors have given approval to the final version of the manuscript. SS, TvE, YO, HJK, MB, NS,
415 BAG, DSD, KM and FD all contributed to aspects of the experiments, analyzed data, wrote and edited
416 the manuscript. SS purified, characterized and prepared samples, SS and TvE processed data and built
417 models, YO performed genetic constructs, MB and DSD conducted computer modeling, HJK, NS
418 and BAG obtained MS data, and KM and FD managed the overall project and supervised the study.

419

Methods

420

421 *Bacterial strains and growth conditions*

422 Bacterial strains, plasmids and primers used are listed in **Table S1**. LB medium supplemented as
423 appropriate with ampicillin, gentamicin, kanamycin or tetracycline at 100, 12, 50 or 12.5 µg/mL,
424 respectively, was used for growing *E. coli* strains at 37 °C. *R. capsulatus* strains were grown
425 chemoheterotrophically under semi-aerobic/dark conditions at 35 °C on enriched (MPYE) medium,
426 supplemented as needed with gentamicin, kanamycin, spectinomycin, or tetracycline at 3, 10, 10 or
427 2.5 µg/mL, respectively. Colonies were stained for *cbb*₃-type CIV activity by incubating plates with
428 a 1:1 (v/v) mixture of 35 mM 1-naphtol and 30 mM N,N-dimethyl-1,4-phenylenediamine (NADI-
429 staining) ⁶¹.

430

431 *Molecular genetic techniques*

432 **Construction of *petABC::ccoP-His*₈ (*cyt bc*₁-*CcoP*) fusion.** Using the primers Fw-ccoP (StuI) and
433 Rv-ccoP (HindIII) (**Table S1**), *petABC::ccoP-His*₈ fusion was constructed by ligating in-frame the PCR amplified
434 1.13 kb *StuI-HindIII* fragment containing *ccoP* (with a C-terminal His₈ tag) to the 3' end of *petABC*, after
435 elimination of the stop codon of *petC* and start codon of *ccoP* on *StuI-HindIII* digested plasmid pMTSI, to yield
436 pYO60 (**Table S1**). The 3.85 kb BamHI fragment of pYO60 carrying *petABC::ccoP* fusion was
437 transferred to the plasmids pBSII and pRK415 using the same sites, yielding pYO63 and pYO76,
438 respectively. The linker-spaced versions of *petABC::ccoP* fusion (*petABC::L2-ccoP*, *petABC::L3-*
439 *ccoP* and *petABC::L4-ccoP*) were also constructed by exchanging the *StuI-HindIII* fragment of pYO63
440 carrying *petABC-ccoP* with the PCR amplified linker added versions, yielding pYO77, pYO78 and
441 pYO80, respectively. L2, L3 and L4 linkers were introduced via the primers F-L2, F-L3 and F-L4
442 (**Table S1**) and contained the amino acid sequences of NH₂-GGSGGGSG-COOH, NH₂-

443 GGSGGGSGGGSG-COOH and NH₂-ASIAGGRTASGP-COOH, respectively. The 3.9 kb KpnI-
444 XbaI fragments carrying these linkers added versions were cloned to pRK415, yielding pYO81,
445 pYO82 and pYO83, respectively. *All constructs were subsequently verified by DNA sequencing. As the protein yields*
446 *and enzymatic activities of all fusion super-complexes (SCs) were similar, only pYO76, which has no linker (i.e., native-like fusion),*
447 *was used for subsequent work.*

448 ***Construction of *petABC::ccoP::cycY-Flag* (*cyt bc₁-CcoP-cyt c_y-Flag*) fusion.*** Using the primers
449 Fw-cp-cy (Ball) and Rv-cp-cy (BglII+HinIII), the C-terminally Flag tagged *cycY* lacking its N-
450 terminal TMH anchor (*i.e.*, amino acid residues 1-30) was PCR amplified. The 619 bp long PCR
451 fragment containing *cycY-Flag* without its anchor was digested with Ball-HinIII and exchanged with
452 its counterpart that encompasses the 3' end of *ccoP* on pYO63 to yield the *petABC::ccoP::cycY-Flag*
453 fusion carried by pYO91. The 4.5 kb KpnI-XbaI fragment of pYO91 containing this fusion was
454 cloned into pRK415 using the same sites to yield pYO92 (Table S1).

455 **Chromosomal inactivation of CIII₂ (*cyt bc₁*) and CIV (*cbb₃-type Cox*) structural genes, and**
456 **construction of strains producing bipartite and tripartite fusion SCs.** The Δ (*petABC::gm*)
457 deletion-insertion allele carried by pYO34³² was transferred using the gene transfer agent (GTA) into
458 the chromosome of *R. capsulatus* strain MG1 (*ccoP::kan*) to yield YO12, providing a mutant
459 background lacking both CIII₂ and the CcoP subunit of CIV. A similar strain, M7G-CBC1 that lacks
460 both CIII₂ and the CcoP subunit but overproduces the CcoN and CcoO subunits of CIV³¹, was also
461 used. The plasmids pYO76 and pYO92 encoding the bipartite and tripartite SCs, respectively, were
462 conjugated into YO12 and M7G-CBC1 using triparental mating to yield pYO76/YO12 and
463 pYO92/M7G-CBC1 strains as in⁶¹ for protein purification.

464

465 ***Purification and characterization of fusion SCs***

466 **Protein purification.** *R. capsulatus* cells (~25-30 g from 8 L media) were resuspended in a final
467 volume of 35-40 mL of buffer A (50 mM Tris-HCl, pH 8.0, 100 mM NaCl, 20 mM EDTA, 1 mM
468 aminocaproic acid and 1 mM 4-(2-Aminoethyl) benzenesulfonyl fluoride hydrochloride (AEBSF)
469 supplemented with Pierce Protease Inhibitor (Thermo Scientific, 1 mini tablet per 30 mL). Cells were
470 disrupted by three passages through a French Pressure Cell (SLM Aminco) at 13,000 psi in the
471 presence of 5-10 mg of DNase I (GoldBio), and cell debris removed by centrifugation at 27,000 x g
472 for 30 min ³¹. Chromatophore membranes were sedimented by centrifugation at 190,000 x g for 2 h
473 and resuspended in buffer A. The protein concentration was determined using the Pierce Protein BCA
474 assay kit (Thermo Scientific), the suspension was supplemented with 10% glycerol and adjusted to a
475 protein concentration of 10 mg/mL with buffer A. Membrane proteins were solubilized with 2% n-
476 dodecyl- β -D-maltoside (DDM, Anatrace) for 15 min on ice, and non-solubilized materials
477 sedimented by centrifugation at 100,000 g for 15 min. The supernatant was subjected to
478 chromatography, as appropriate.

479 The His-tagged bipartite SC was purified by anion exchange chromatography on Bio-Gel A-50
480 (Bio-Rad), followed by affinity chromatography on Ni-Sepharose High Performance (GE
481 Healthcare). Solubilized proteins were loaded onto a 40 mL Bio-Gel column equilibrated with Tris
482 buffer (50 mM Tris-HCl, pH 8.0, 100 mM NaCl, 1% glycerol and 0.01% DDM) and washed with
483 three column volumes (CV) of the buffer. After another washing step with 3 CV of Tris buffer
484 containing 150 mM NaCl to eliminate weakly bound proteins elution was carried out with a linear,
485 five CV gradient from 150-400 mM NaCl in Tris buffer. Fractions containing both cyt *c* reductase
486 and cyt *c* oxidase activities were combined and loaded onto a 7 mL Ni-Sepharose column equilibrated
487 with the binding buffer (50 mM Tris-HCl, pH 8.0, 500 mM NaCl, 20 mM imidazole, 1% glycerol and
488 0.01% DDM). After washing with 30 mL of binding buffer, the column was eluted with a linear 100
489 mL gradient from 20-260 mM imidazole.

490 The Flag-tagged tripartite SC was purified by affinity chromatography using the Anti-Flag affinity
491 gel (Bimake). The supernatant containing solubilized proteins was loaded onto a 1 mL column
492 equilibrated with TBS buffer (50 mM Tris-HCl, pH 7.4, 150 mM NaCl, 0.01% DDM and 1 mM
493 AEBSF), washed with 10 ml TBS and eluted with 5 mL of Flag (DYKDDDDK) peptide (100 µg/mL)
494 (Sigma) in TBS buffer.

495 Eluted proteins were concentrated (Amicon Ultra-15, 30 kDa MWCO) (Millipore) to a final
496 volume of 150-200 µL and loaded onto a Superose 6 Increase 10/300 GL (GE Healthcare) size
497 exclusion column equilibrated with TBS buffer, and eluted with the same buffer at a flow rate of 0.4
498 mL/min. Peak fractions were combined and concentrated, and PD MiniTrap G-25 columns (GE
499 Healthcare) were used for buffer exchanges, as needed.

500 **Protein analyses.** Native PAGE was performed using 4-13% gels⁶², and SDS-PAGE used 12.5%
501 or 18% gels⁶³. Gels were stained with Coomassie Brilliant Blue (Bio-Rad) or colloidal silver⁶⁴.
502 Immunoblot analyses were performed using polyclonal antibodies specific of *R. capsulatus* cyt *b*²⁸
503 and monoclonal anti-rabbit-IgG-alkaline phosphatase (Sigma) used at 1:10.000 dilution. CIV in-gel
504 activity was revealed by incubating native gels with 0.5 mg/ml 3,3'-diaminobenzidine in 50 mM Na-
505 phosphate, pH 7.2⁶⁵. The *c*-type cyts were revealed by their heme peroxidase activity, using 3,3',5,5'-
506 tetramethylbenzidine (TMBZ) and hydrogen peroxide (H₂O₂)⁶⁶. Briefly, gels were washed with 0.25
507 M Na-acetate buffer (pH 5) and incubated with 6.3 mM TMBZ in 30% methanol, 0.25 M Na-acetate,
508 pH 5.0. After 1 h incubation, 0.4% H₂O₂ were added to reveal the peroxidase activity of *c*-type cyts.

509 Reduced *minus* oxidized spectra were recorded in 50 mM MOPS, pH 7.0 using a Cary 60 UV-
510 Vis spectrophotometer (Agilent). Usually, 50 µg of purified protein was first fully oxidized by adding
511 a grain of K₃[Fe(CN)₆] and then gradually reduced with a few grains of sodium ascorbate or sodium
512 dithionite, as appropriate. Protein concentrations were determined with a NanoDrop 2000c (Thermo
513 Scientific) using the A₂₈₀ method⁶⁷.

514 **Enzyme activities.** Cyt *c* reductase (cyt *bc*₁) activity was determined as described⁶⁸. Briefly, 10
515 mM stock solution of 2,3-dimethoxy-5-methyl-6-decyl-1,4-benzoquinone (DB) (Sigma) in DMSO
516 was reduced to DBH₂ with a few grains of sodium borohydride and excess borohydride was quenched
517 by adding HCl to a final pH of 6.0. For assays, 40 μM DBH₂ were added to 25 μM horse heart cyt *c*
518 (Sigma) in 500 μL assay buffer (40 mM sodium phosphate, pH 7.4, 20 mM sodium malonate, 0.5
519 mM EDTA, 0.5 mM KCN and 0.01% DDM) in a stirred cuvette, and the non-enzymatic rate of cyt *c*
520 reduction was recorded at 550 nm for 1 min (Cary 60 UV-Vis spectrophotometer, Agilent). The
521 reaction was initiated by adding 1-2 μg of purified protein and cyt *c* reduction was monitored. The
522 enzymatic activity was inhibited by adding 1 μM stigmatellin (Fluka), a specific inhibitor of cyt *bc*₁-
523 type CIII₂.

524 The CIV (cyt *cbb*₃-Cox) activity was determined as described⁶⁹. Reduced horse heart cyt *c*
525 (Sigma) was prepared by incubating a 1-2 mM stock solution with 10 mM sodium dithionite for 15
526 min at room temperature, excess dithionite was removed by gel filtration using a PD-10 desalting
527 column (GE Healthcare), and the final concentration of reduced cyt *c* was calculated based on its
528 absorption at 550 nm and an $\epsilon=20 \text{ mM}^{-1}\text{cm}^{-1}$. 20 μM reduced cyt *c* in 500 μL assay buffer (10 mM
529 Tris-HCl, pH 7.0, 100 mM KCl) were prepared in a stirred cuvette (Cary 60 UV-Vis
530 spectrophotometer), and the baseline was recorded for 1 min. The reaction was started by adding 1-2
531 μg of purified protein, and cyt *c* oxidation monitored at 550 nm. The enzymatic activity was inhibited
532 by addition of 250 μM KCN as an inhibitor of *cbb*₃-Cox.

533 DBH₂ dependent oxygen consumption was monitored using a mini Clark-type oxygen electrode
534 (Instech Laboratories, PA) at 25 °C. The assay was performed in the same buffer as that used for cyt
535 *c* reductase activity (40 mM sodium phosphate, pH 7.4, 20 mM sodium malonate, 0.5 mM EDTA and
536 0.01% DDM), but without KCN. A baseline was recorded after adding 100 μM DBH₂ to 1 mL of
537 assay buffer, and the reaction started by adding 30 μg of purified protein. As needed, purified protein

538 was pre-incubated with a 1:1 (w/w) mixture of *E. coli* polar lipids (Avanti), which improved the
539 activity. 20 μM horse heart cyt *c* (Sigma), 250 μM KCN or 1 μM of stigmatellin were used as
540 specificity controls.

541 **Identification of protein subunits by mass spectrometry.** Protein bands from gels were excised,
542 and after reduction (dithiothreitol; Sigma) and alkylation (iodoacetamide; Bio-Rad) subjected to in-
543 gel trypsin digestion (Promega, Sequencing Grade Modified Trypsin) overnight at 37 °C. Peptides
544 eluted from the gel samples were dried, desalted using ZipTips (Millipore U-C18 P10, Millipore),
545 lyophilized and stored at -80 °C. They were resuspended in 10 μL 5% acetonitrile/0.1% formic acid
546 prior to MS, using either a LCQ Deca XP+ ion trap, or a Q-Exactive Quadrupole-Orbitrap mass
547 spectrometer (both from Thermo Fisher Scientific)⁷⁰. The LCQ Deca XP+ mass spectrometer was
548 coupled to a Thermo-Dionex LC Packings Ultimate Nano HPLC system controlled by Thermo
549 Xcalibur version 2.0 software. Peptides were separated on a 15 cm C18 nanocolumn (Thermo-
550 Dionex, NAN-75-15-03-PM) using a 45-min linear gradient from 4% to 40% buffer B (100%
551 acetonitrile, 0.1% formic acid), followed by a 7-min gradient from 40% to 80% buffer B and 8-min
552 wash with 80% B (constant flow rate 150 $\text{nL}\cdot\text{min}^{-1}$). MS/MS data were acquired in data-dependent
553 analysis mode with dynamic exclusion enabled (repeat count: 3, exclusion duration: 3 min). Full MS
554 survey scans (mass range 300–2000 m/z) were followed by MS/MS fragmentation (normalized
555 collision energy 35) of the top 3 most intense ions. The Q-Exactive Quadrupole-Orbitrap mass
556 spectrometer was coupled to an Easy-nLC™ 1000 nano HPLC (Thermo Fisher Scientific), and
557 samples were loaded in buffer A (0.1% formic acid) onto a 20-cm-long fused silica capillary column
558 (75 μm ID), packed with reversed-phase Repro-Sil Pur C18-AQ 3 μm resin (Dr. Maisch GmbH,
559 Ammerbuch, Germany). Peptides were eluted using a 45-min linear gradient from 4% to 40% buffer
560 B (100% acetonitrile, 0.1% formic acid), followed by a 7-min gradient from 40% to 80% buffer B
561 and 8-min wash with 80% B (constant flow rate 300 $\text{nL}\cdot\text{min}^{-1}$). The Q-Exactive was operated in data-

562 dependent acquisition mode with dynamic exclusion enabled (repeat count: 1, exclusion duration: 20
563 s). Full MS survey scans (mass range 300–1600 m/z) at high resolution (70 000 at 200 m/z) were
564 followed by MS/MS fragmentation of the top 15 most intense ions with higher energy collisional
565 dissociation at a normalized collision energy of 22 (resolution 17 500 at 200 m/z). Dual lock mass
566 calibration was enabled with 371.101233 and 445.120024 m/z background ions.

567 MS spectra were searched against the *R. capsulatus* protein database (<https://www.uniprot.org>,
568 last modified 01/15/2020; *Rhodobacter capsulatus* (strain ATCC BAA-309 / NBRC 16581 /
569 SB1003)) using Proteome Discoverer 1.4 (Thermo Fisher Scientific) with Sequest-HT search engine.
570 Search parameters were set to full trypsin digestion, with maxima of three missed cleavages and three
571 modifications per peptide. Oxidation of methionine (+16 Da) and carbamidomethylation of cysteine
572 (+57 Da) were selected as dynamic modifications. Precursor and fragment ion tolerances were set to
573 2 Da and 1 Da, respectively, for the LCQ DecaXP+, and 10 ppm and 0.6 Da, respectively, for the Q-
574 Exactive data. False discovery rates by target-decoy search (FDR) were set to 0.01 and X_{corr} filter
575 based on charge (z) were: > 2 for $z = 2$; > 2.5 for $z = 3$; and > 2.6 for $z = 4$ ⁷⁰. All identifications are
576 listed in **Table S2**.

577

578 ***Binding of cyt c_y , soluble variant of cyt c_y (cyt S- c_y) and cyt c_2 to purified proteins***

579 **Cyt c_y and cyt S- c_y .** Binding of purified cyt c_y ⁷¹, or a variant of it containing only the soluble cyt
580 domain (cyt S- c_y) (residues 99-199) to the bipartite SC was assayed by mixing a 5-10 fold molar
581 excess of purified cyt c with 125 μg of purified SC in a final volume of 150 μL TBS buffer (50 mM
582 Tris-HCl, pH 7.4, 150 mM NaCl and 0.01% DDM). The mixture was separated by chromatography
583 using Superose 6 Increase size exclusion column, and elution fractions were analyzed by SDS-PAGE
584 followed by silver staining. Cyt S- c_y was purified from the *R. capsulatus* strain pYO135/FJ2-R4
585 (**Table S1**) grown under photosynthetic conditions to maximize its yield³². Cells were washed with

586 20 mM Tris-HCl, pH 8.0 and resuspended 1:5 (w/v) in the same buffer supplemented with 50 mM
587 NaCl. Polymyxin B sulfate (1 mg/mL) was added, and the cell suspension incubated for 75 min on
588 ice with gentle stirring. After centrifugation for 20 min at 10,000 g followed by 3 h at 150,000 g, the
589 supernatant was collected and concentrated to a final volume of 2 ml (Amicon Ultra-15 3 kDa
590 MWCO) (Millipore). Aliquots of 300 μ L were loaded onto Superose 6 Increase (GE Healthcare)
591 equilibrated in 30 mM Tris-HCl, pH 8.0 and eluted in the same buffer. Fractions eluting after 20 mL
592 were combined and concentrated using Amicon Ultra-15 3 kDa MWCO filters (Millipore).

593 **Cyt c_2 .** Binding of cyt c_2 to *cbb*₃-type CIV was determined by mixing 2-fold molar excess of
594 purified *R. capsulatus* cyt c_2 ⁷² with 300 μ g of purified CIV³¹ under low-salt conditions (20 mM Tris-
595 HCl, pH 7.4, 1 mM NaCl and 0.01% DDM). The mixture (250 μ L total volume) was loaded onto a
596 Superose 6 Increase (GE Healthcare) sizing column equilibrated with the same buffer to separate the
597 proteins. Elution fractions were concentrated (Amicon Ultra-15, 3 kDa MWCO) (Millipore) and a
598 volume containing 1 to 5 μ g of protein was analyzed by SDS-PAGE followed by silver staining.

599

600 ***Protein cross-linking and mass spectrometry***

601 **Protein cross-linking using chemical crosslinkers.** 180 μ g of purified bipartite SC at a
602 concentration of 1 mg/mL in PBS buffer (50 mM Na-Phosphate, pH 7.4, 150 mM NaCl and 0.01%
603 DDM) mixed with 5-fold molar excess (90 μ g) of purified cyt c_y ⁷¹ were supplemented with 6 mM
604 disuccinimidyl dibutyric urea (DSBU) (Thermo Fisher Scientific), and incubated on ice for 2 h. The
605 reaction was quenched by adding 50 mM of ammonium bicarbonate, and the mixture analyzed by
606 mass spectrometry. 300 μ g of purified *cbb*₃-type CIV³¹ were mixed with a 2-fold molar excess of
607 purified cyt c_2 ⁷² at a final protein concentration of 200 μ g/mL under low-salt conditions (20 mM Na-
608 phosphate, pH 7.4, 1 mM NaCl and 0.01% DDM), and incubated with 20 mM 4-(4,6-Dimethoxy-
609 1,3,5-triazin-2-yl)-4-methylmorpholinium chloride (DMTMM) (Sigma) for 1 h at room temperature.

610 Similarly, 300 μg of purified bc_1 -type CIII₂ were mixed with 2-fold molar excess of purified cyt c_2 ,
611 and treated with DMTMM as above. In both cases, the reaction was stopped by removing excess
612 DMTMM with a PD MiniTrap G-25 desalting column (GE Healthcare), and crosslinked proteins
613 were precipitated with 20% (w/v) trichloroacetic acid (TCA, Sigma) at 4°C for 1 h. Proteins were
614 pelleted by centrifugation at 21,000 x g for 15 min and washed with 10% TCA in 0.1 M Tris-HCl and
615 then with acetone (Fisher). The solvent was discarded, the pellet air-dried and then stored at -80°C
616 for analysis by mass spectrometry.

617 **Mass spectrometry of crosslinked proteins.** Crosslinked proteins were resuspended in an
618 appropriate volume of solution A (2.5% TCA, 50 mM SDS and 50 mM triethylammonium
619 bicarbonate (TEAB) final concentrations) and reduced with 10 mM DTT (US Biological) for 30 min
620 at 30 °C, followed by alkylation with 50 mM iodoacetamide (Sigma Aldrich) for 30 min at 30 °C. The
621 proteins were processed using an S-Trap™ according to the protocol recommended by the supplier
622 (Protifi, C02-mini), and digested with trypsin (Thermo Fisher Scientific) in 1:10 (w/w)
623 enzyme/protein ratio for 1 h at 30 °C. Peptides eluted from this column were vacuum-dried and
624 resuspended with the peptide fractionation-elution buffer for LC-MS [(70% (v/v) LC-MS grade water
625 (Thermo Fisher Scientific), 30% (v/v) acetonitrile (ACN, Thermo Fisher Scientific) and 0.1 % (v/v)
626 trifluoroacetic acid (TFA, Thermo Fisher Scientific)]. Peptides were first fractionated using AKTA
627 Pure 25 with Superdex 30 Increase 3.2/300 (GE Life Science) at a flow rate of 30 $\mu\text{L min}^{-1}$ of the
628 elution buffer, and 100 μL fractions were collected. Based on the elution profile, fractions containing
629 enriched crosslinked peptides of higher molecular masses, were vacuum-dried and resuspended with
630 LC-MS grade water containing 0.1% (v/v) TFA for mass spectrometry analysis. One half of each
631 fraction was analyzed by a Q-Exactive HF mass spectrometer (Thermo Fisher Scientific) coupled to
632 a Dionex Ultimate 3000 UHPLC system (Thermo Fischer Scientific) equipped with an in-house made
633 15 cm long fused silica capillary column (75 μm ID), packed with reversed-phase Repro-Sil Pur C18-

634 AQ 2.4 μm resin (Dr. Maisch GmbH, Ammerbuch, Germany). Elution was performed using a
635 gradient from 5% to 45% B (90 min), followed by 90% B (5 min), and re-equilibration from 90% to
636 5% B (5 min) with a flow rate of 400 nL/min (mobile phase A: water with 0.1% formic acid; mobile
637 phase B: 80% acetonitrile with 0.1% formic acid). Data were acquired in data-dependent MS/MS
638 mode. Full scan MS settings were: mass range 300–1800 m/z, resolution 120,000; MS1 AGC target
639 1E6; MS1 Maximum IT 200. MS/MS settings were: resolution 30,000; AGC target 2E5; MS2
640 Maximum IT 300 ms; fragmentation was enforced by higher-energy collisional dissociation with
641 stepped collision energy of 25, 27, 30; loop count top 12; isolation window 1.5; fixed first mass 130;
642 MS2 Minimum AGC target 800; charge exclusion: unassigned, 1, 2, 3, 8 and >8; peptide match off;
643 exclude isotope on; dynamic exclusion 45 sec³⁹. Raw files were converted to mgf format with
644 TurboRawToMGF 2.0.8⁷³.

645 **Crosslinked peptide searches.** MeroX 2.0.0.5⁴⁰, FindXL⁴² and MassAI 19.07
646 (<http://www.massai.dk>) were used to identify and validate crosslinked peptides, and only those that
647 were consistently identified by two different search engines (MeroX and FindXL for DMTMM, and
648 MeroX and MassAI for DSBU) were used for method validation and docking experiments. MeroX
649 was run in RISEUP mode, with default crosslinker mass and fragmentation parameters for DSBU,
650 and in Quadratic mode with default crosslinker mass parameters for DMTMM; precursor mass range,
651 300–10,000 Da; minimum precursor charge 4; precursor and fragment ion precisions 5.0 and 10.0
652 ppm, respectively; maximum number of missed cleavages 3; carbamidomethylation of cysteine and
653 oxidation of methionine, as fixed and variable modifications, respectively; results were filtered for
654 score (>10) and false discovery rate, FDR (<1%). FindXL was used to analyze and validate MeroX
655 results for DMTMM crosslinks. The default FindXL parameters were used as described before⁴² with
656 the possible crosslink amino acids adjustments for K, Y, S, or T on one peptide, and E or D on the
657 other peptide. MassAI was used to validate crosslinks identified by MeroX for DSBU with standard

658 settings, except: 5 ppm MS accuracy, 0.05 Da MS/MS accuracy, 3 allowed missed cleavages, and
659 carbamidomethylation of cysteine and oxidation of methionine, as fixed and variable modifications,
660 respectively. Visualization of the crosslinks in the structures used Chimera ⁷⁴ with the Xlink Analyzer
661 plug-in ⁷⁵.

662

663 *Negative staining and cryo-EM sample preparation*

664 For negative staining, purified SCs were diluted to 0.01-0.05 mg/mL concentrations in TBS (50 mM
665 Tris-HCl, pH 7.4, 150 mM NaCl, 0.01% DDM and 1 mM AEBSF) buffer, 5 μ L applied to glow-
666 discharged (20 sec, 25 mA, Pelco easiGlow) carbon-coated Cu grids (CF300-CU, EMS), incubated
667 for 1 min and stained with 2% uranyl acetate. Grids were imaged on FEI Tecnai 12 transmission
668 electron microscope operating at 120 kV, with a CCD camera (Gatan BM-Ultrascan).

669 For cryo-EM, the tripartite SC was used as purified, whereas the purified bipartite SC was mixed
670 with a 5-fold molar excess of purified cyt *c*_y ⁷¹. 2.5 μ L of the mixture, containing 3-5 mg/mL proteins,
671 were applied to CFlat holey carbon grids (1.2/1.3-400 mesh or 2/2-300 mesh) (EMS), which were
672 glow discharged (2 min, 25 mA, Pelco easiGlow) before sample application. Grids were blotted for
673 9 sec at force 0 (CFlat-1.2/1.3), or for 3 sec at force -5 (CFlat-2/2), and flash-frozen in liquid ethane
674 cooled with liquid nitrogen using FEI Vitrobot Mark IV (25°C, 100% humidity). Plunge freezing
675 conditions were optimized using FEI Tecnai TF20 TEM operating at 200 kV, equipped with a FEI
676 Falcon II camera.

677

678 *Cryo-EM data acquisition and processing*

679 All cryo-EM grids were imaged using FEI Titan Krios electron microscope operating at 300 kV.
680 Images of the tripartite SC (SC~*c*_y) were recorded using a Gatan K2 Summit direct electron detector,
681 equipped with an energy quantum filter (20 eV), and operated in super-resolution mode at a nominal

682 magnification of 105,000x, resulting in a binned pixel size of 1.32 Å. Images were dose-fractionated
683 to 40 frames with a total exposure time of 10 sec, and a total dose of 40 e-/Å². Automated data
684 acquisition was carried out using Latitude software (Gatan), and nominal defocus values varied from
685 1 to 2.5 μm. Movies were motion corrected using MotionCor2 ⁷⁶ and CTF parameters were
686 determined with CTFFIND 4.1 ⁷⁷. About 10,000 particles were manually picked and subjected to an
687 initial reference-free 2D classification using Relion 3.0 ⁷⁸. Representative classes were selected and
688 used as a template for auto-picking. After sorting and two rounds of 2D classification, ~30,000
689 particles were retained from the dataset. For 3D classification, an initial model was created using *R.*
690 *capsulatus* CIII₂ structure (PDB: 1ZRT) and low-pass filtered to 60 Å using EMAN2 ⁷⁹. A 3D map
691 with a nominal resolution of ~11 Å containing a total of ~12,000 particles (40%) was obtained,
692 showing a CIII₂ associated on one side with a single copy of CIV. For further analyses, additional
693 datasets were collected using samples from the same batch and identical imaging conditions. From a
694 total of ~17,000 images, ~1,000,000 particles were automatically picked using the template obtained
695 from the first dataset, and after sorting and two rounds of 2D classification, ~500,000 particles were
696 retained. Various subsets of all images were processed separately, and yielded the same overall results
697 with slightly different versions of individual maps. For clarity, only the paths to the best representative
698 of each of the final maps are shown (**Fig. S2A, B and C**). For 3D classification, the map obtained
699 from the first dataset (**Fig. S2, Box 3**) was low-pass filtered to 60 Å and used as the initial model. Of
700 the five classes obtained, one showed clear features of a CIII₂ dimer associated with a single monomer
701 of CIV (**Fig. S2, class005 in A, class002 in B and C**). The remaining classes showed the same overall
702 shape, but lacked density or resolution in different parts of the structure. Only two of the five maps
703 contained a second monomer of CIV associated with the other monomer of CIII₂ (**Fig. S2C**). These
704 two classes showing this feature were combined, yielding a subset of ~ 220,000 particles. These
705 particles were further processed by another round of 2D classification, and subjected to 3D

706 classification, yielding three classes (**Fig. S2C**). Only one of the maps obtained in this second round
707 of 3D classification clearly showed density for a second monomer of CIV. Aligned particles from this
708 group were subclassified into six classes in another round of 3D classification using a soft mask and
709 no image alignment. The low number of particles (~5,000) per class limited the resolution of the maps
710 ($< 10\text{\AA}$), and could not be further improved through 3D refinement.

711 Refinement of the individual maps (**Fig. S2A,B**) led to relatively low resolution reconstructions,
712 particularly in the CIV portion of the map, probably due to greater structural heterogeneity in the
713 sample with respect to this portion of the tripartite SC. The highest resolution was obtained with a
714 map containing a single copy of CIV, by combining all classes showing well defined features
715 corresponding to it and subjecting them to a second round of 3D classification, focused on CIV
716 portion of the map. For this purpose, a soft mask around CIV was created by fitting the closely related
717 structure of *P. stutzeri* (PDB: 3MK7) into the map and low-pass filtering it to 10 \AA . All information
718 outside of this mask was subtracted from the aligned particles, and the remaining particles were
719 subjected to a masked classification without image alignment, to yield six classes (**Fig. S2A**).
720 Alternatively, a cylindrical mask was wrapped around the CIV portion of the map and used in a
721 similar procedure (**Fig. S2B**). In each case, classes showing the highest level of details were retained,
722 and the entire unsubtracted particles dataset subjected to 3D auto-refinement followed by per-particle
723 CTF refinement, Bayesian polishing and post-processing using Relion 3.0. The two extreme
724 conformations of the orientation of CIV relative to CIII₂ were represented by the maps SC-1A and
725 SC-1B (**Fig. S2A,B**), which were refined to 6.1 \AA and 7.2 \AA resolutions, respectively (**Table S3**).

726 Images of the bipartite SC supplemented with cyt *c_y* (SC+*c_y*) were recorded by a Gatan K3 direct
727 electron detector equipped with an energy quantum filter (20 eV) and operated in counting mode at a
728 nominal magnification of 64,000x, corresponding to a pixel size of 1.36 \AA . Images were dose-
729 fractionated to 80 frames with a total exposure time of 3.1 sec and a total dose of 40 e⁻/ \AA^2 . Nominal

730 defocus values varied from 1 to 2.5 μm . Automated data acquisition was carried out using Latitude
731 software (Gatan) and image shift ($\sim 2 \mu\text{m}$, 4 images per stage position) was used for accelerated data
732 collection. For this sample 5,480 images were collected in the first session, motion corrected using
733 MotionCor2 ⁷⁶, and CTF parameters were determined with CTFFIND 4.1 ⁷⁷. For auto-picking, the
734 template previously obtained with the tripartite SC was used, with this and all subsequent steps done
735 in Relion 3.0 ⁷⁸. After sorting and two rounds of 2D classification, $\sim 228,000$ particles were retained
736 (**Fig. S5A**). The same initial model as for the tripartite SC was used for 3D classification into five
737 classes. Two classes (001 and 002) resembled more to the overall shape of a CIII₂ without CIV, while
738 the other three classes showed the same overall shape of a CIII₂CIV SC, as seen with the tripartite
739 sample. 37,460 particles corresponding to the SC class with the highest level of detail were combined
740 with SC particles from the second dataset (**Fig. S5B**) to yield the best final map of the bipartite SC.
741 The second dataset consisted of 12,200 images which were collected and processed under the same
742 conditions as the first dataset. 1.6 million particles were auto-picked and after two rounds of 2D
743 classification, classes were split into $\sim 340,000$ large particles likely representing CIII₂CIV and
744 $\sim 465,000$ particles resembling CIII₂ (**Fig. S5B,D**). The former particles were subjected to 3D
745 classification into three classes, and the class most similar to the overall shape of CIII₂CIV was
746 identified. It contained $\sim 118,000$ particles, but due to its low level of detail, it was subjected to another
747 round of 2D classification. The 34,819 particles thus retained were combined with 37,460 SC particles
748 from the first dataset (**Fig. S5A**). After 3D classification into five classes, the class with the highest
749 level of detail contained 56% of particles, and clearly showed the overall shape of CIII₂CIV. 41,017
750 aligned particles corresponding to this class were extracted and subjected to a second round of 3D
751 classification without image alignment using a soft mask. Of the six 3D classes, the one with the
752 highest nominal resolution contained 14,978 particles (36%) and was subjected to 3D auto-refinement
753 and post processing, followed by per-particle CTF refinement and Bayesian polishing. After a second

754 round of 3D auto-refinement and post processing, the final map (SC-2A) of the bipartite CIII₂CIV
755 was obtained at a nominal resolution of 5.18 Å (**Table S3**). This map was very similar to that (SC-
756 1A) of the tripartite CIII₂CIV, except for its higher resolution and strongly improved density and
757 resolution of the extra TMHs at the interface. Unlike the tripartite samples, no major class
758 corresponding to the conformation seen in SC-1B was identified.

759 As the bipartite SC samples contained a significant amount of CIII₂ particles without CIV, subsets
760 of smaller 2D classes consistent with a CIII₂ dimer were selected and processed separately. Of the
761 ~376,000 total particles retained from the dataset 1, ~267,000 were identified as resembling CIII₂.
762 After a second round of 2D classification (**Fig. S5C**), ~213,000 particles were retained and used to
763 generate an *ab initio* 3D model. This model was lowpass filtered to 60 Å and used as initial model
764 for the 3D classification of ~465,000 CIII₂ particles from dataset 2 (**Fig. S5D**). Particles corresponding
765 to the class with the highest resolution and level of detail (~185,000) were combined with the CIII₂
766 particles from dataset 1 to yield ~400,000 particles, and subjected to 3D classification. The ~170,000
767 particles corresponding to the best class were further processed following two different strategies.
768 CIII₂ being a homodimer based on X-ray structures, C2 symmetry was applied in the next round of
769 3D classification and in all subsequent steps (**Fig. S5E**). The best class contained ~120,000 particles
770 (70%) which were extracted and, similar to CIII₂CIV, subjected to another round of 3D classification
771 without image alignment using a soft mask. Of the six classes obtained, some showed the external
772 domain (ED) of both monomers of the FeS protein close to heme b_L (“**b** position”, b-b) while other
773 classes showed both EDs close to heme c_1 (“**c** position”, c-c). Individual classes were subjected to 3D
774 auto-refinement and post processing, followed by two rounds of per-particle CTF refinement,
775 Bayesian polishing, 3D auto-refinement and post processing. Only the final map with the highest
776 nominal resolution (3.30Å) is shown (**Fig. S5E**, CIII₂) (**Table S3**). This map contained 37,997
777 particles and showed both FeS-EDs close to b position, but at a lower local resolution and occupancy

778 than the rest of the map, indicating structural flexibility and conformational heterogeneity. A similar
779 approach was used in **Fig. S5F**, except that no C2 symmetry was applied in the two rounds of 3D
780 classifications. Of the three best classes obtained in the second round, one showed both EDs in the b
781 position, one showed both in the c position, and one showed a heterodimeric conformation with one
782 monomer in the b and the other in the c position. Each of the maps was further processed as in **Fig.**
783 **S5E**, but C2 symmetry was only applied in case of the homodimeric structures. The final maps were
784 CIII₂ c-c with both ED's in the c position at 3.8Å, CIII₂ b-b with both ED's in the b position at 3.5Å,
785 and CIII₂ b-c with one ED in the b and the second in the c position at 4.2Å (**Table S3**). The nominal
786 resolutions thus obtained were slightly lower than in map CIII₂ (**Fig. S5E**). However, by omitting C2
787 symmetry application to the 3D classifications, the conformational heterogeneity of the FeS protein
788 EDs was resolved, and a subset of particles showing a heterodimeric conformation was identified.
789 The different locations (*i.e.*, b or c positions) of the ED's were clear in the three maps (**Fig. S5F**) but
790 their occupancy and local resolutions was lower than the rest of the structure.

791 A third dataset was also collected and yielded ~303,000 particles after the first 2D classification.
792 Adding these particles to the first two datasets did not improve the maps shown in **Fig. S5A,B**, but it
793 turned out to be informative. As shown in **Fig. S5G**, particles from dataset 3 were subjected to two
794 rounds of 3D classification. Interestingly, an extra density near the periplasmic domain of CcoP, could
795 be seen in some classes. This was not observed in any subclass obtained from the datasets 1 and 2,
796 and tentatively thought to correspond to the cyt c domain of cyt c_y. Focused classification followed
797 by 3D auto-refinement and post processing, using wider soft masks around the periplasmic domain
798 of CcoP to avoid cutting-off any of the extra density, led to a final map (SC-2B) with limited
799 resolution (10.5Å), and could not be further improved by sub-classification due to the low number of
800 particles in each subclass.

801

802 ***Refinement of R. capsulatus CIII₂ in the cryo-EM maps***

803 The X-ray based structure of *R. capsulatus* CIII₂ (PDB: 1ZRT) was fitted into map CIII₂ (EMD-
804 22189) which had the highest nominal resolution of all maps obtained (**Fig. S5E**), and refined using
805 Phenix1.16⁸⁰. The real space refinement approach included four rounds of global minimization, local
806 grid search, morphing and simulated annealing, with the final round also including ADP (B-factor)
807 refinement. Each round included 5 cycles using default settings, and morphing and annealing were
808 performed in each cycle. Secondary structures were determined by Phenix1.16, using default search
809 settings and restrictions were applied during real space refinement. Due to the low occupancy and
810 limited local resolution, the FeS-ED proteins (residues 50-191) were only subjected to rigid body
811 fitting followed by two rounds of global minimization and local grid search (5 cycles each), but not
812 to morphing and simulated annealing. To ensure the correct cofactor geometry, hemes and [2Fe-2S]
813 clusters including their coordinating residues were copied from the high-resolution X-ray structure of
814 the homologous CIII₂ (cyt *bc*₁) from *R. sphaeroides* (PDB: 6NHH). Validation was performed using
815 MolProbity⁸¹ (<http://molprobity.biochem.duke.edu/>), and outliers (Ramachandran, rotamer, bonds,
816 angles) were manually corrected in Coot⁸², using real space refinement and regularization. The model
817 that was refined in map CIII₂ (EMD-22189) was subsequently used for rigid body fitting into the
818 maps CIII₂ b-b, CIII₂ c-c and CIII₂ b-c (**Fig. S5F**) (**Table S3**). Each chain was treated as one separate
819 body, except the FeS protein, which was split into its TMH (11 to 49) and ED (50 to 191) residues.
820 After the procedure, the linker region between the ED and TMH (residues 40-50) was remodeled in
821 Coot using real space refinement and regularization.

822

823 ***Structural modeling of R. capsulatus cbb₃-type CIV subunits, CcoH and cyt c_γ***

824 **Modeling of *R. capsulatus* cbb₃-type CIV.** The *Pseudomonas stutzeri* cbb₃-type CIV structure (PDB:
825 5DJQ) (sequence identities for *R. capsulatus* CcoN: 68%, CcoO: 55%, CcoP: 34%) was used as a

826 template, and comparative models were computed using MODELLER v9.18⁸³ with defined
827 secondary structure and crosslinking restraints. The secondary structures for the regions without any
828 template coverage (CcoP residues 104 to 112, 176 to 178, 184 to 197 and 204 to 215; CcoO residues
829 172 to 185 and 192 to 199), due to the insertion sequences that are present only in *R. capsulatus* CIV,
830 were estimated using PsiPred Protein Sequence Analysis Workbench^{84,85}, and added as restraints to
831 MODELLER. Cross-link distances were added as Gaussian restraints to MODELLER with a mean
832 of 18.0Å and a standard deviation of 1.0Å. Problematic loop regions (a total of ten loops longer than
833 four amino acids) were detected by MolProbity^{81,86} and remodeled using MODELLER “slow”
834 refinement method (**Table S3**). As *R. capsulatus* CcoN is longer than that of *P. stutzeri* with a
835 predicted extra N-ter TMH, whereas CcoP is shorter with only one predicted N-ter TMH instead of
836 two, these regions were not included into the model. The regions CcoO 179-214 as well as CcoP 1-
837 12, 53-59, 161-173 and 272-280 without template coverage that were not supported by the cryo-EM
838 maps were omitted.

839 **Modeling of CcoH and cyt *c* domain of *c_γ*.** For CcoH (residues Met 1 to Thr35) five *ab initio*
840 models were obtained using I-TASSER server⁸⁷. All models were almost identical, and one with the
841 lowest energy score was retained. For *R. capsulatus* cyt *c_γ*, its homologs with known structures were
842 detected using HHpred⁸⁸, and the structure of cyt *c* domain of cyt *c*₅₅₂ from *Paracoccus denitrificans*
843 (PDB: 3M97; sequence identity: 61%) was used as a template for the soluble cyt *c* domain of *c_γ* and
844 comparative models were computed using MODELLER⁸³.

845 **Modeling of the extra N-ter TMH of CcoN (TMH0).** A 29-residue model consisting of CcoN
846 residues Arg25 to Asp53, which includes the predicted transmembrane region (Met30-Leu48,
847 UniProtKB, D5ARP4), was obtained from the I-TASSER server⁸⁹. The alpha helical region included
848 residues Leu27 to Thr50, and the model including the residues Arg25 to Leu48 was manually fitted
849 into the density map for visualization purpose in **Fig. 2**. Corresponding coordinates were not

850 deposited in the PDB because the registration could not be determined due to the lack of side chain
851 density.

852 **Modeling of cyt c_y and CcoH TMHs interactions.** The 30 residues long cyt c_y TMH was
853 manually docked into the density map by positioning Phe15 and Tyr21 into the corresponding
854 densities, and refined by real-space refinement and regularization using Coot. The I-TASSER model
855 of CcoH was docked into the map by moving it along the corresponding density, retaining its close
856 association with cyt c_y TMH. The best fit was found when Ala23 and Val24 of CcoH were located at
857 the interface with cyt c_y TMH. The interaction of the two helices was optimized by GalaxyWEB⁹⁰,
858 and the model with the lowest energy profile was refined in map SC-2A using Phenix 1.17. The
859 refinement strategy included 5 cycles of global minimization, rigid body fitting (where cyt c_y and
860 CcoH chains were treated as separate bodies), local grid search and ADP (B-factor) refinement with
861 default settings for all steps. Secondary structure restrictions were applied to the α -helical parts of
862 CcoH as predicted by I-TASSER (residues 12 to 34) and to cyt c_y as predicted by GalaxyWEB
863 (residues 2 to 9 and 12 to 29). CIII₂ and CIV models were present during the refinement to keep the
864 rest of the map occupied, but changes made during this procedure were discarded as these models
865 were refined separately.

866 **Integrative modeling and docking CcoH, cyt c_y and cyt c_2 to bipartite SC.** The entire SC was
867 assembled by an integrative modeling approach using the cryo-EM map, XL-MS, co-evolutionary
868 analysis, and subunit models described above. CIII₂ and CIV models were fitted into the cryo-EM
869 maps in UCSF Chimera⁷⁴. Additional data about the interaction interfaces between the different
870 subunits were obtained using RaptorX-ComplexContact³³ for each pair of the SC subunits. Based on
871 co-evolution and machine learning, this method predicted the pairs of residues that are in contact. The
872 PatchDock, which is an efficient rigid docking method that maximizes geometric shape
873 complementarity³⁴, was used to generate docked configurations of CcoH, cyt c_2 and cyt c_y to CIII₂

874 and CIV, as appropriate. The different subunits were docked in parallel and independently from each
875 other.

876 **Docking of CcoH to CIV.** A total of 16 contacts predicted by RaptorX-ComplexContact, with
877 probabilities higher than 0.5, were used as distance restraints for protein-protein docking³⁴. The
878 models satisfied 13 of the contacts, and a single cluster of docked models evidenced by the
879 convergence of the top 100 results, was obtained (**Fig. S7**). This cluster coincided with the additional
880 feature seen at the SC interface, and CcoH TMH was modelled into this feature.

881 **Docking of cyt c_2 to CIII₂ and CIV.** *R. capsulatus* cyt c_2 of known structure (PDB: 1C2N) was
882 docked to CIII₂ using the three distance restraints between cyt c_2 and cyt c_1 derived from the protein
883 cross-linking data (**Table S4**). Similarly, cyt c_2 was docked to CIV using nine distance restraints
884 provided by XLs (1 crosslink to CcoP and 8 to CcoO, **Table S4**). The models yielded one main cluster
885 in each case, and covered 100% and 89% of the data for CIII₂ and CIV, respectively.

886 **Docking of cyt c_y to CIII₂CIV SC.** The model of cyt c domain of c_y was docked by PatchDock
887 to bipartite CIII₂CIV, which has both FeS-EDs of CIII₂ in the b position. Ten distance restraints
888 derived from the XL-MS data (6 with DMTMM and 4 with DSBU, **Table S4**) were used, yielding
889 two main clusters (1 and 2) of the docked models on the p side of CIII₂ (**Fig. S4**), and satisfied 100%
890 of the restraints. As the cryo-EM data revealed that CIII₂ particles could have their FeS-EDs in the c
891 position, the corresponding CIII₂ c-c, CIII₂ b-b and CIII₂ b-c models were used for docking via
892 Patchdock the cyt c domain of c_y onto CIII₂.

893 All the models were ranked using statistically optimized atomic potentials (SOAP)⁹¹, and those
894 that have low SOAP scores were retained.

895

896 **References**

- 897 1 Nicholls, D. G. & Ferguson, S. J. *Bioenergetics 4*. (Elsevier, 2013).
- 898 2 Darrouzet, E., Moser, C. C., Dutton, P. L. & Daldal, F. Large scale domain movement in
899 cytochrome *bc*₁: a new device for electron transfer in proteins. *Trends Biochem Sci* **26**, 445-451,
900 doi:10.1016/s0968-0004(01)01897-7 (2001).
- 901 3 Esser, L. *et al.* Surface-modulated motion switch: capture and release of iron-sulfur protein in the
902 cytochrome *bc*₁ complex. *Proc Natl Acad Sci U S A* **103**, 13045-13050,
903 doi:10.1073/pnas.0601149103 (2006).
- 904 4 Khalfaoui-Hassani, B. *et al.* in *Cytochrome Complexes: Evolution, Structures, Energy*
905 *Transduction, and Signaling*. (eds W. Cramer & T. Kallas) 527-555 (Springer, 2016).
- 906 5 Smith, M. A., Finel, M., Korolik, V. & Mendz, G. L. Characteristics of the aerobic respiratory
907 chains of the microaerophiles *Campylobacter jejuni* and *Helicobacter pylori*. *Arch Microbiol* **174**,
908 1-10, doi:10.1007/s002030000174 (2000).
- 909 6 Aspholm, M. *et al.* Structural alterations in a component of cytochrome *c* oxidase and molecular
910 evolution of pathogenic *Neisseria* in humans. *PLoS Pathog* **6**, e1001055,
911 doi:10.1371/journal.ppat.1001055 (2010).
- 912 7 Ekici, S., Pawlik, G., Lohmeyer, E., Koch, H. G. & Daldal, F. Biogenesis of *cbb(3)*-type
913 cytochrome *c* oxidase in *Rhodobacter capsulatus*. *Biochim Biophys Acta* **1817**, 898-910,
914 doi:10.1016/j.bbabi.2011.10.011 (2012).
- 915 8 Jenney, F. E., Jr. & Daldal, F. A novel membrane-associated *c*-type cytochrome, *cyt c_y*, can
916 mediate the photosynthetic growth of *Rhodobacter capsulatus* and *Rhodobacter sphaeroides*.
917 *EMBO J* **12**, 1283-1292 (1993).
- 918 9 Turba, A., Jetzek, M. & Ludwig, B. Purification of *Paracoccus denitrificans* cytochrome *c*₅₅₂ and
919 sequence analysis of the gene. *Eur J Biochem* **231**, 259-265 (1995).
- 920 10 Albert, I., Rutherford, A. W., Grav, H., Kellermann, J. & Michel, H. The 18 kDa cytochrome *c*₅₅₃
921 from *Heliobacterium gestii*: gene sequence and characterization of the mature protein.
922 *Biochemistry* **37**, 9001-9008, doi:10.1021/bi9731347 (1998).
- 923 11 Kim, M. S. *et al.* Isolation and Characterization of a Hybrid Respiratory Supercomplex Consisting
924 of *Mycobacterium tuberculosis* Cytochrome *bcc* and *Mycobacterium smegmatis* Cytochrome *aa*₃.
925 *J Biol Chem* **290**, 14350-14360, doi:10.1074/jbc.M114.624312 (2015).
- 926 12 Winstedt, L. & von Wachenfeldt, C. Terminal oxidases of *Bacillus subtilis* strain 168: one quinol
927 oxidase, cytochrome *aa*₃ or cytochrome *bd*, is required for aerobic growth. *J Bacteriol* **182**, 6557-
928 6564, doi:10.1128/jb.182.23.6557-6564.2000 (2000).
- 929 13 Hochkoeppler, A., Jenney, F. E., Jr., Lang, S. E., Zannoni, D. & Daldal, F. Membrane-associated
930 cytochrome *c_y* of *Rhodobacter capsulatus* is an electron carrier from the cytochrome *bc*₁ complex
931 to the cytochrome *c* oxidase during respiration. *J Bacteriol* **177**, 608-613,
932 doi:10.1128/jb.177.3.608-613.1995 (1995).
- 933 14 Enriquez, J. A. Supramolecular Organization of Respiratory Complexes. *Annu Rev Physiol* **78**,
934 533-561, doi:10.1146/annurev-physiol-021115-105031 (2016).
- 935 15 Melo, A. M. & Teixeira, M. Supramolecular organization of bacterial aerobic respiratory chains:
936 From cells and back. *Biochim Biophys Acta* **1857**, 190-197, doi:10.1016/j.bbabi.2015.11.001
937 (2016).
- 938 16 Brzezinski, P. New Structures Reveal Interaction Dynamics in Respiratory Supercomplexes.
939 *Trends Biochem Sci*, doi:10.1016/j.tibs.2019.10.011 (2019).

- 940 17 Letts, J. A., Fiedorczuk, K., Degliesposti, G., Skehel, M. & Sazanov, L. A. Structures of
941 Respiratory Supercomplex I+III₂ Reveal Functional and Conformational Crosstalk. *Mol Cell* **75**,
942 1131-1146 e1136, doi:10.1016/j.molcel.2019.07.022 (2019).
- 943 18 Quintana-Cabrera, R. & Soriano, M. E. ER Stress Priming of Mitochondrial Respiratory
944 suPERKomplex Assembly. *Trends Endocrinol Metab* **30**, 685-687,
945 doi:10.1016/j.tem.2019.08.003 (2019).
- 946 19 Letts, J. A., Fiedorczuk, K. & Sazanov, L. A. The architecture of respiratory supercomplexes.
947 *Nature* **537**, 644-648, doi:10.1038/nature19774 (2016).
- 948 20 Gu, J. *et al.* The architecture of the mammalian respirasome. *Nature* **537**, 639-643,
949 doi:10.1038/nature19359 (2016).
- 950 21 Hartley, A. M. *et al.* Structure of yeast cytochrome *c* oxidase in a supercomplex with cytochrome
951 *bc*₁. *Nat Struct Mol Biol* **26**, 78-83, doi:10.1038/s41594-018-0172-z (2019).
- 952 22 Berry, E. A. & Trumpower, B. L. Isolation of ubiquinol oxidase from *Paracoccus denitrificans*
953 and resolution into cytochrome *bc*₁ and cytochrome *c-aa*₃ complexes. *J Biol Chem* **260**, 2458-
954 2467 (1985).
- 955 23 Kao, W. C. *et al.* The obligate respiratory supercomplex from *Actinobacteria*. *Biochim Biophys*
956 *Acta* **1857**, 1705-1714, doi:10.1016/j.bbabi.2016.07.009 (2016).
- 957 24 Gong, H. *et al.* An electron transfer path connects subunits of a mycobacterial respiratory
958 supercomplex. *Science* **362**, doi:10.1126/science.aat8923 (2018).
- 959 25 Wiseman, B. *et al.* Structure of a functional obligate complex III₂IV₂ respiratory supercomplex
960 from *Mycobacterium smegmatis*. *Nat Struct Mol Biol* **25**, 1128-1136, doi:10.1038/s41594-018-
961 0160-3 (2018).
- 962 26 Ducluzeau, A. L., Ouchane, S. & Nitschke, W. The *cbb*₃ oxidases are an ancient innovation of the
963 domain bacteria. *Mol Biol Evol* **25**, 1158-1166, doi:10.1093/molbev/msn062 (2008).
- 964 27 Myllykallio, H., Drepper, F., Mathis, P. & Daldal, F. Electron-transfer supercomplexes in
965 photosynthesis and respiration. *Trends Microbiol* **8**, 493-494, doi:10.1016/s0966-842x(00)01831-
966 x (2000).
- 967 28 Davidson, E., Ohnishi, T., Tokito, M. & Daldal, F. *Rhodobacter capsulatus* mutants lacking the
968 Rieske FeS protein form a stable cytochrome *bc*₁ subcomplex with an intact quinone reduction
969 site. *Biochemistry* **31**, 3351-3358, doi:10.1021/bi00128a007 (1992).
- 970 29 Kulajta, C., Thumfart, J. O., Haid, S., Daldal, F. & Koch, H. G. Multi-step assembly pathway of
971 the *cbb*₃-type cytochrome *c* oxidase complex. *J Mol Biol* **355**, 989-1004,
972 doi:10.1016/j.jmb.2005.11.039 (2006).
- 973 30 Valkova-Valchanova, M. B., Saribas, A. S., Gibney, B. R., Dutton, P. L. & Daldal, F. Isolation
974 and characterization of a two-subunit cytochrome *b-c*₁ subcomplex from *Rhodobacter capsulatus*
975 and reconstitution of its ubihydroquinone oxidation (Q_o) site with purified Fe-S protein subunit.
976 *Biochemistry* **37**, 16242-16251, doi:10.1021/bi981651z (1998).
- 977 31 Gray, K. A. *et al.* *Rhodobacter capsulatus* contains a novel *cb*-type cytochrome *c* oxidase without
978 a Cu_A center. *Biochemistry* **33**, 3120-3127, doi:10.1021/bi00176a047 (1994).
- 979 32 Ozturk, Y. *et al.* Soluble variants of *Rhodobacter capsulatus* membrane-anchored cytochrome *c*_y
980 are efficient photosynthetic electron carriers. *J Biol Chem* **283**, 13964-13972,
981 doi:10.1074/jbc.M800090200 (2008).
- 982 33 Zeng, H. *et al.* ComplexContact: a web server for inter-protein contact prediction using deep
983 learning. *Nucleic Acids Res* **46**, W432-W437, doi:10.1093/nar/gky420 (2018).
- 984 34 Schneidman-Duhovny, D., Inbar, Y., Nussinov, R. & Wolfson, H. J. PatchDock and SymmDock:
985 servers for rigid and symmetric docking. *Nucleic Acids Res* **33**, W363-367,
986 doi:10.1093/nar/gki481 (2005).

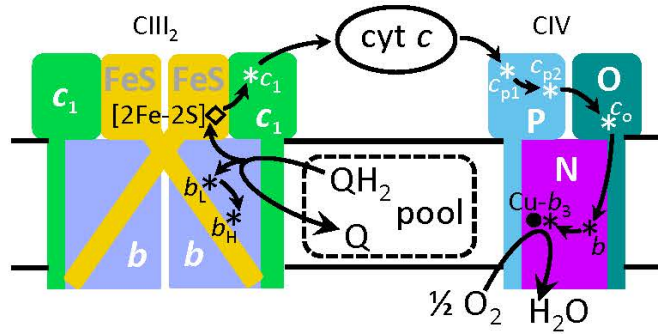
- 987 35 Pawlik, G. *et al.* The putative assembly factor CcoH is stably associated with the *cbb*₃-type
988 cytochrome oxidase. *J Bacteriol* **192**, 6378-6389, doi:10.1128/JB.00988-10 (2010).
- 989 36 Covian, R. & Trumpower, B. L. Rapid electron transfer between monomers when the cytochrome
990 *bc*₁ complex dimer is reduced through center N. *J Biol Chem* **280**, 22732-22740,
991 doi:10.1074/jbc.M413592200 (2005).
- 992 37 Castellani, M. *et al.* Direct demonstration of half-of-the-sites reactivity in the dimeric cytochrome
993 *bc*₁ complex: enzyme with one inactive monomer is fully active but unable to activate the second
994 ubiquinol oxidation site in response to ligand binding at the ubiquinone reduction site. *J Biol*
995 *Chem* **285**, 502-510, doi:10.1074/jbc.M109.072959 (2010).
- 996 38 Cooley, J. W., Lee, D. W. & Daldal, F. Across membrane communication between the Q_o and Q_i
997 active sites of cytochrome *bc*₁. *Biochemistry* **48**, 1888-1899, doi:10.1021/bi802216h (2009).
- 998 39 Slavin, M. & Kalisman, N. Structural Analysis of Protein Complexes by Cross-Linking and Mass
999 Spectrometry. *Methods Mol Biol* **1764**, 173-183, doi:10.1007/978-1-4939-7759-8_11 (2018).
- 1000 40 Gotze, M. *et al.* Automated assignment of MS/MS cleavable cross-links in protein 3D-structure
1001 analysis. *J Am Soc Mass Spectrom* **26**, 83-97, doi:10.1007/s13361-014-1001-1 (2015).
- 1002 41 Solmaz, S. R. & Hunte, C. Structure of complex III with bound cytochrome *c* in reduced state and
1003 definition of a minimal core interface for electron transfer. *J Biol Chem* **283**, 17542-17549,
1004 doi:10.1074/jbc.M710126200 (2008).
- 1005 42 Kalisman, N., Adams, C. M. & Levitt, M. Subunit order of eukaryotic TRiC/CCT chaperonin by
1006 cross-linking, mass spectrometry, and combinatorial homology modeling. *Proc Natl Acad Sci U*
1007 *S A* **109**, 2884-2889, doi:10.1073/pnas.1119472109 (2012).
- 1008 43 Iacobucci, C. *et al.* A cross-linking/mass spectrometry workflow based on MS-cleavable cross-
1009 linkers and the MeroX software for studying protein structures and protein-protein interactions.
1010 *Nat Protoc* **13**, 2864-2889, doi:10.1038/s41596-018-0068-8 (2018).
- 1011 44 Osyczka, A., Moser, C. C. & Dutton, P. L. Fixing the Q cycle. *Trends Biochem Sci* **30**, 176-182,
1012 doi:10.1016/j.tibs.2005.02.001 (2005).
- 1013 45 Crofts, A. R. *et al.* The Q-cycle reviewed: How well does a monomeric mechanism of the *bc*(1)
1014 complex account for the function of a dimeric complex? *Biochim Biophys Acta* **1777**, 1001-1019,
1015 doi:10.1016/j.bbabi.2008.04.037 (2008).
- 1016 46 Buschmann, S. *et al.* The structure of *cbb*₃ cytochrome oxidase provides insights into proton
1017 pumping. *Science* **329**, 327-330, doi:10.1126/science.1187303 (2010).
- 1018 47 Myllykallio, H., Drepper, F., Mathis, P. & Daldal, F. Membrane-anchored cytochrome *c*_γ
1019 mediated microsecond time range electron transfer from the cytochrome *bc*₁ complex to the
1020 reaction center in *Rhodobacter capsulatus*. *Biochemistry* **37**, 5501-5510, doi:10.1021/bi973123d
1021 (1998).
- 1022 48 Lee, D. W., Ozturk, Y., Osyczka, A., Cooley, J. W. & Daldal, F. Cytochrome *bc*₁-*c*_γ fusion
1023 complexes reveal the distance constraints for functional electron transfer between photosynthesis
1024 components. *J Biol Chem* **283**, 13973-13982, doi:10.1074/jbc.M800091200 (2008).
- 1025 49 Berry, E. A. *et al.* X-Ray Structure of *Rhodobacter capsulatus* Cytochrome *bc*₁: Comparison with
1026 its Mitochondrial and Chloroplast Counterparts. *Photosynth Res* **81**, 251-275,
1027 doi:10.1023/B:PRES.0000036888.18223.0e (2004).
- 1028 50 Xia, D. *et al.* The road to the crystal structure of the cytochrome *bc*₁ complex from the anoxygenic,
1029 photosynthetic bacterium *Rhodobacter sphaeroides*. *J Bioenerg Biomembr* **40**, 485-492,
1030 doi:10.1007/s10863-008-9180-8 (2008).
- 1031 51 Esser, L. *et al.* Inhibitor-complexed structures of the cytochrome *bc*₁ from the photosynthetic
1032 bacterium *Rhodobacter sphaeroides*. *J Biol Chem* **283**, 2846-2857, doi:10.1074/jbc.M708608200
1033 (2008).

- 1034 52 Sousa, J. S., Mills, D. J., Vonck, J. & Kuhlbrandt, W. Functional asymmetry and electron flow in
1035 the bovine respirasome. *Elife* **5**, doi:10.7554/eLife.21290 (2016).
- 1036 53 Swierczek, M. *et al.* An electronic bus bar lies in the core of cytochrome bc_1 . *Science* **329**, 451-
1037 454, doi:10.1126/science.1190899 (2010).
- 1038 54 Lanciano, P., Lee, D. W., Yang, H., Darrouzet, E. & Daldal, F. Intermonomer electron transfer
1039 between the low-potential b hemes of cytochrome bc_1 . *Biochemistry* **50**, 1651-1663,
1040 doi:10.1021/bi101736v (2011).
- 1041 55 Moser, C. C., Keske, J. M., Warncke, K., Farid, R. S. & Dutton, P. L. Nature of biological electron
1042 transfer. *Nature* **355**, 796-802, doi:10.1038/355796a0 (1992).
- 1043 56 Wikstrom, M., Krab, K. & Sharma, V. Oxygen Activation and Energy Conservation by
1044 Cytochrome c Oxidase. *Chem Rev* **118**, 2469-2490, doi:10.1021/acs.chemrev.7b00664 (2018).
- 1045 57 Brzezinski, P. & Gennis, R. B. Cytochrome c oxidase: exciting progress and remaining mysteries.
1046 *J Bioenerg Biomembr* **40**, 521-531, doi:10.1007/s10863-008-9181-7 (2008).
- 1047 58 Verissimo, A. F., Sousa, F. L., Baptista, A. M., Teixeira, M. & Pereira, M. M. Thermodynamic
1048 redox behavior of the heme centers of cbb_3 heme-copper oxygen reductase from *Bradyrhizobium*
1049 *japonicum*. *Biochemistry* **46**, 13245-13253, doi:10.1021/bi700733g (2007).
- 1050 59 Otten, M. F. *et al.* Cytochromes c_{550} , c_{552} , and c_1 in the electron transport network of *Paracoccus*
1051 *denitrificans*: redundant or subtly different in function? *J Bacteriol* **183**, 7017-7026,
1052 doi:10.1128/JB.183.24.7017-7026.2001 (2001).
- 1053 60 Kappler, U. & Dahl, C. Enzymology and molecular biology of prokaryotic sulfite oxidation.
1054 *FEMS Microbiol Lett* **203**, 1-9, doi:10.1111/j.1574-6968.2001.tb10813.x (2001).
- 1055 61 Khalfaoui-Hassani, B. *et al.* Widespread Distribution and Functional Specificity of the Copper
1056 Importer CcoA: Distinct Cu Uptake Routes for Bacterial Cytochrome c Oxidases. *MBio* **9**,
1057 doi:10.1128/mBio.00065-18 (2018).
- 1058 62 Wittig, I., Braun, H. P. & Schagger, H. Blue native PAGE. *Nat Protoc* **1**, 418-428,
1059 doi:10.1038/nprot.2006.62 (2006).
- 1060 63 Laemmli, U. K. Cleavage of structural proteins during the assembly of the head of bacteriophage
1061 T4. *Nature* **227**, 680-685, doi:10.1038/227680a0 (1970).
- 1062 64 Bartsch, H., Arndt, C., Koristka, S., Cartellieri, M. & Bachmann, M. Silver staining techniques of
1063 polyacrylamide gels. *Methods Mol Biol* **869**, 481-486, doi:10.1007/978-1-61779-821-4_42
1064 (2012).
- 1065 65 Yan, L. J. & Forster, M. J. Resolving mitochondrial protein complexes using nongradient blue
1066 native polyacrylamide gel electrophoresis. *Anal Biochem* **389**, 143-149,
1067 doi:10.1016/j.ab.2009.03.043 (2009).
- 1068 66 Thomas, P. E., Ryan, D. & Levin, W. An improved staining procedure for the detection of the
1069 peroxidase activity of cytochrome P-450 on sodium dodecyl sulfate polyacrylamide gels. *Anal*
1070 *Biochem* **75**, 168-176, doi:10.1016/0003-2697(76)90067-1 (1976).
- 1071 67 Gill, S. C. & von Hippel, P. H. Calculation of protein extinction coefficients from amino acid
1072 sequence data. *Anal. Biochem.* **182**, 319-326 (1989).
- 1073 68 Atta-Asafo-Adjei, E. & Daldal, F. Size of the amino acid side chain at position 158 of cytochrome
1074 b is critical for an active cytochrome bc_1 complex and for photosynthetic growth of *Rhodobacter*
1075 *capsulatus*. *Proc Natl Acad Sci U S A* **88**, 492-496, doi:10.1073/pnas.88.2.492 (1991).
- 1076 69 Peters, A., Kulajta, C., Pawlik, G., Daldal, F. & Koch, H. G. Stability of the cbb_3 -type cytochrome
1077 oxidase requires specific CcoQ-CcoP interactions. *J Bacteriol* **190**, 5576-5586,
1078 doi:10.1128/JB.00534-08 (2008).

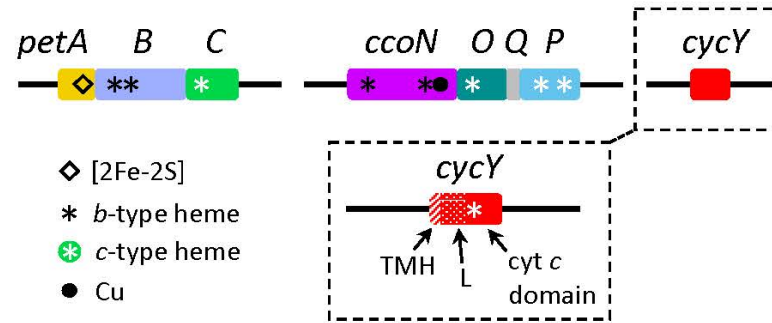
- 1079 70 Selamoglu, N. *et al.* Comparative differential cuproproteomes of *Rhodobacter capsulatus* reveal
1080 novel copper homeostasis related proteins. *Metallomics* **12**, 572-591, doi:10.1039/c9mt00314b
1081 (2020).
- 1082 71 Myllykallio, H., Jenney, F. E., Jr., Moomaw, C. R., Slaughter, C. A. & Daldal, F. Cytochrome *c*₁
1083 of *Rhodobacter capsulatus* is attached to the cytoplasmic membrane by an uncleaved signal
1084 sequence-like anchor. *J Bacteriol* **179**, 2623-2631, doi:10.1128/jb.179.8.2623-2631.1997 (1997).
- 1085 72 Holden, H. M., Meyer, T. E., Cusanovich, M. A., Daldal, F. & Rayment, I. Crystallization and
1086 preliminary analysis of crystals of cytochrome *c*₂ from *Rhodospseudomonas capsulata*. *J Mol Biol*
1087 **195**, 229-231, doi:10.1016/0022-2836(87)90341-x (1987).
- 1088 73 Sheng, Q. *et al.* Preprocessing significantly improves the peptide/protein identification sensitivity
1089 of high-resolution isobarically labeled tandem mass spectrometry data. *Mol Cell Proteomics* **14**,
1090 405-417, doi:10.1074/mcp.O114.041376 (2015).
- 1091 74 Pettersen, E. F. *et al.* UCSF Chimera--a visualization system for exploratory research and
1092 analysis. *J Comput Chem* **25**, 1605-1612, doi:10.1002/jcc.20084 (2004).
- 1093 75 Kosinski, J. *et al.* Xlink Analyzer: software for analysis and visualization of cross-linking data in
1094 the context of three-dimensional structures. *J Struct Biol* **189**, 177-183,
1095 doi:10.1016/j.jsb.2015.01.014 (2015).
- 1096 76 Zheng, S. *et al.* MotionCor2: anisotropic correction of beam-induced motion for improved cryo-
1097 electron microscopy. *Nat Methods* **14**, 331-332, doi:10.1038/nmeth.4193 (2017).
- 1098 77 Rohou, A. & Grigorieff, N. CTFFIND4: fast and accurate defocus estimation from electron
1099 micrographs. *J. Struct. Biol.* **192**, 216-221 (2015).
- 1100 78 Zivanov, J. *et al.* New tools for automated high-resolution cryo-EM structure determination in
1101 RELION-3. *eLife* **7:e42166**, doi:10.7554/eLife.42166 (2018).
- 1102 79 Tang, G. *et al.* EMAN2: An extensible image processing suite for electron microscopy. *J. Struct.*
1103 *Biol.* **157**, 38-46 (2007).
- 1104 80 Liebschner, D. *et al.* Macromolecular structure determination using X-rays, neutrons and
1105 electrons: recent developments in Phenix. *Acta Crystallogr D Struct Biol* **75**, 861-877,
1106 doi:10.1107/S2059798319011471 (2019).
- 1107 81 Williams, C. J. *et al.* MolProbity: More and better reference data for improved all-atom structure
1108 validation. *Protein Sci* **27**, 293-315, doi:10.1002/pro.3330 (2018).
- 1109 82 Emsley, P., Lohkamp, B., Scott, W. G. & Cowtan, K. Features and development of Coot. *Acta*
1110 *Crystallogr D Biol Crystallogr* **66**, 486-501, doi:10.1107/S0907444910007493 (2010).
- 1111 83 Webb, B. & Sali, A. Comparative Protein Structure Modeling Using MODELLER. *Curr Protoc*
1112 *Bioinformatics* **47**, 5 6 1-32, doi:10.1002/0471250953.bi0506s47 (2014).
- 1113 84 Buchan, D. W. A. & Jones, D. T. The PSIPRED Protein Analysis Workbench: 20 years on.
1114 *Nucleic Acids Res* **47**, W402-W407, doi:10.1093/nar/gkz297 (2019).
- 1115 85 Jones, D. T., Tress, M., Bryson, K. & Hadley, C. Successful recognition of protein folds using
1116 threading methods biased by sequence similarity and predicted secondary structure. *Proteins*
1117 **Suppl 3**, 104-111, doi:10.1002/(sici)1097-0134(1999)37:3+<104::aid-prot14>3.3.co;2-g (1999).
- 1118 86 Chen, V. B. *et al.* MolProbity: all-atom structure validation for macromolecular crystallography.
1119 *Acta Crystallogr D Biol Crystallogr* **66**, 12-21, doi:10.1107/S0907444909042073 (2010).
- 1120 87 Yang, J. *et al.* The I-TASSER Suite: protein structure and function prediction. *Nat Methods* **12**,
1121 7-8, doi:10.1038/nmeth.3213 (2015).
- 1122 88 Soding, J. Protein homology detection by HMM-HMM comparison. *Bioinformatics* **21**, 951-960,
1123 doi:10.1093/bioinformatics/bti125 (2005).
- 1124 89 Zhang, W. *et al.* Integration of QUARK and I-TASSER for Ab Initio Protein Structure Prediction
1125 in CASP11. *Proteins* **84 Suppl 1**, 76-86, doi:10.1002/prot.24930 (2016).

- 1126 90 Ko, J., Park, H., Heo, L. & Seok, C. GalaxyWEB server for protein structure prediction and
1127 refinement. *Nucleic Acids Res* **40**, W294-297, doi:10.1093/nar/gks493 (2012).
- 1128 91 Dong, G. Q., Fan, H., Schneidman-Duhovny, D., Webb, B. & Sali, A. Optimized atomic statistical
1129 potentials: assessment of protein interfaces and loops. *Bioinformatics* **29**, 3158-3166,
1130 doi:10.1093/bioinformatics/btt560 (2013).
- 1131

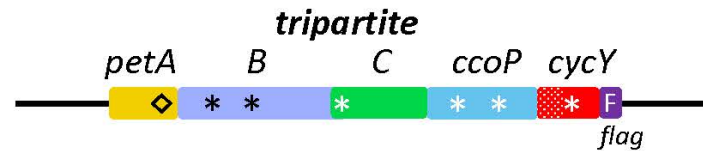
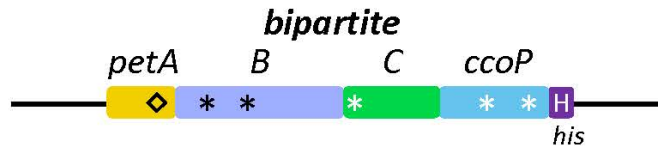
A e⁻ transfer from CIII to CIV



B Genes on chromosome



C Gene fusions on plasmid



D CIII-CIV super-complexes (SC)

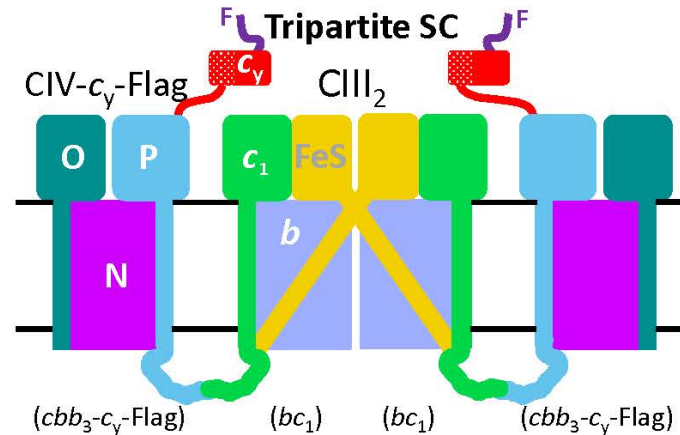
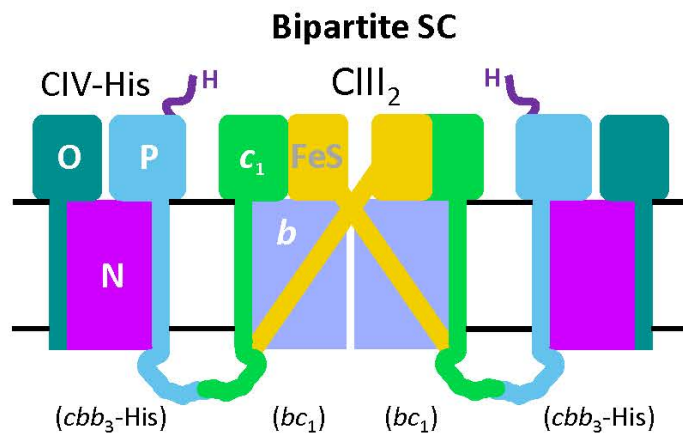


Figure 1. Steimle et al.,

1133 **Figure 1. QH₂ oxidation and fused SCs. A.** Oxidation of QH₂ to Q by CIII₂ and reduction of O₂ to H₂O by CIV. A bifurcated electron
1134 transfer reaction conveys one electron from QH₂ to the [2Fe-2S] cluster of the FeS protein (FeS, yellow), and another electron to hemes *b_L*
1135 and *b_H* of cyt *b* (periwinkle). Reduced [2Fe-2S] cluster transfers the electron to heme *c₁* on cyt *c₁* (green), via the movement of the FeS
1136 protein from near heme *b_L* to near heme *c₁*. The subsequent electron transfer step from heme *b_H* to Q from the pool to form a SQ
1137 (semiquinone) is not shown for clarity. A cyt *c* (*c₂* or *c_y*) carries electrons from heme *c₁* to CIV, where electrons reach the heme-Cu (Cu-
1138 *b₃*) site, where O₂ is reduced to H₂O, via the hemes *c_{p1}* and *c_{p2}* of CcoP (P, light blue), *c_o* of CcoO (O, dark green) and heme *b* of CcoN (N,
1139 purple). **B.** *R. capsulatus* genes used for fused SCs. *petABC* encodes the structural genes of the *bc₁*-type CIII₂ subunits, the FeS protein
1140 (*petA*, yellow), cyt *b* (*B*, periwinkle) and cyt *c₁* (*C*, green). *ccoNOQP* encodes the structural genes of the *cbb₃*-type CIV subunits, the CcoN
1141 (*ccoN*, purple), CcoO (*O*, dark green), CcoQ (*Q*, grey) and CcoP (*P*, light blue). *cycY* gene (red) encodes the membrane-anchored cyt *c_y*,
1142 and its 30-residue transmembrane helix (TMH), 69-residue linker (L) and 100-residue cyt *c* (cyt *c*) domain are indicated. Heme cofactors
1143 of *b*- and *c*-type cyts are indicated by black and white asterisks, respectively, whereas diamond and dot designate the [2Fe-2S] cluster and
1144 Cu atom, respectively. **C.** Plasmid-borne genetic fusions. The bipartite fusion (left) is formed by in-frame linking the 3'-end of *petC* to the
1145 5'-end of *ccoP*, and the tripartite fusion (right) by adding the linker and cyt *c* domain of *cycY* to the 3'-end of *ccoP*. Colors and cofactor
1146 symbols are as in **A**, and the His (H) and Flag (F) affinity tags (dark purple) at the 3'-end of the bipartite and tripartite fusion subunits are
1147 shown. **D.** Schematic depiction of bipartite (left) and tripartite (right) super-complexes (SC). The bipartite SC encodes a CIII₂ dimer fused
1148 on each side to a His-tagged CIV. The tripartite SC also contains the Flag-tagged cyt domain of *c_y* (red) at the end of CcoP (blue).

1149

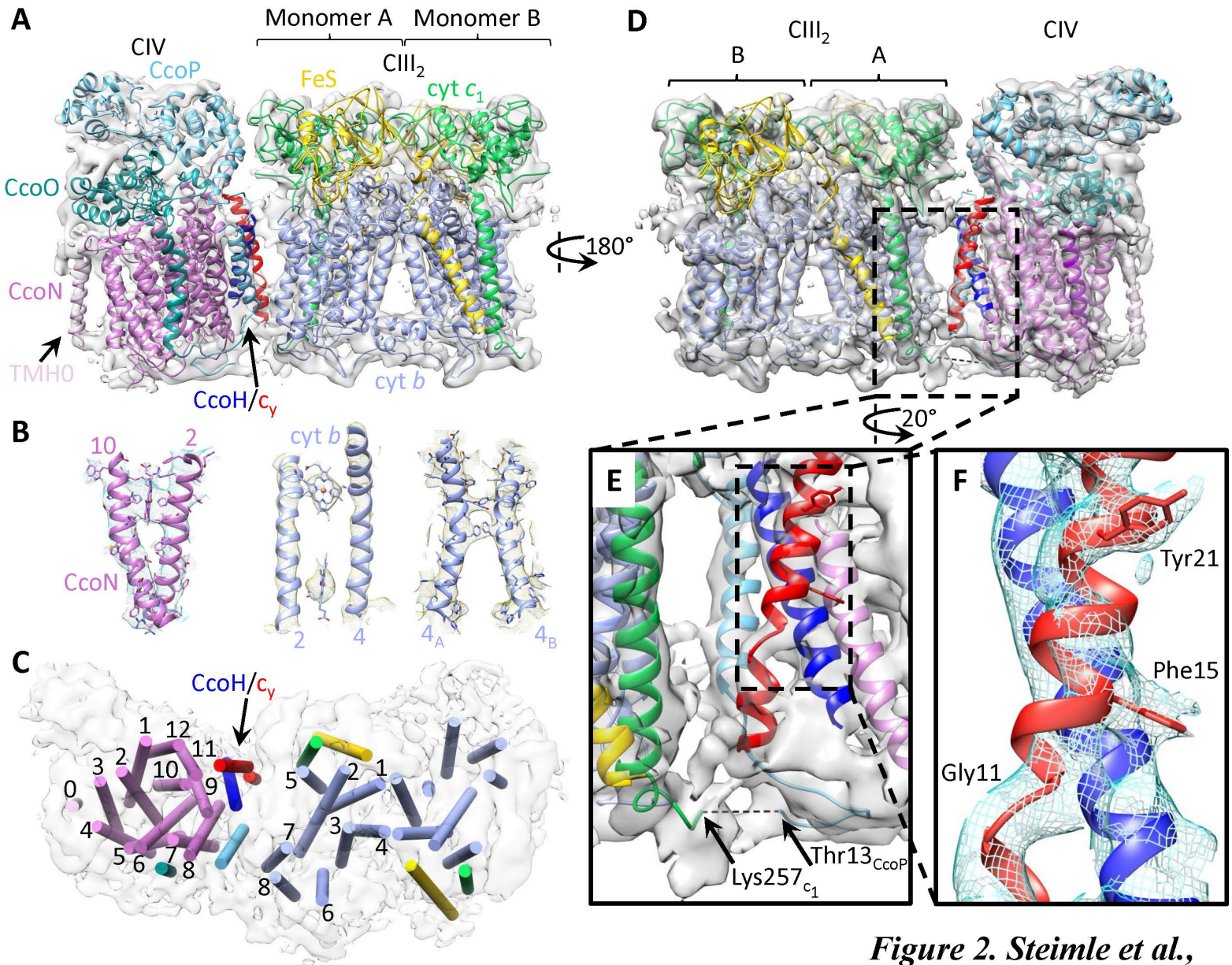


Figure 2. Steimle et al.,

1151 **Figure 2. Cryo-EM structure of CIII₂CIV.** **A.** Side view of CIII₂CIV. The structures of CIII₂ (PDB: 6XI0), and the homology model of
1152 *R. capsulatus cbb₃*-type CIV were fitted into the cryo-EM map SC-2A depicted in transparent grey. All subunits are colored and labelled
1153 as indicated, and the additional feature indicated by an arrow at the edge of CcoN subunit of CIV corresponds to the extra N-ter TMH
1154 (TMH0, light purple) specific to *R. capsulatus*. The large arrow points out the CcoH/*c_y* helices in red/blue. **B.** Representative regions of
1155 the cryo-EM map showing the map quality and model fitting. The TMH2 and TMH10 of CcoN (left) show clearly heme *b* and some bulky
1156 side chains. Only the protein backbone and hemes *b_L* and *b_H* are resolved between the TMH2 and TMH4 of cyt *b* (center) (see **Fig. 3B** for
1157 comparison with CIII₂ map at 3.3 Å). Large side chains are clearly visible between the TMH4 of monomer A and TMH4 of monomer B of
1158 CIII₂ (4_A and 4_B, respectively; right). **C.** Top view of CIII₂CIV with TMHs depicted as cylinders and colored as in **A**. The TMHs of cyt *b*
1159 (only CIII₂ monomer A) and CcoN of CIV are numbered, and the TMHs of the FeS protein (yellow), cyt *c₁* (green), CcoO (dark green),
1160 CcoP (light blue), CcoH/*c_y* (blue/red with an arrow) and CcoN TMH0 (light purple) are shown. **D.** 180° rotated view for the back view of
1161 CIII₂CIV interface. The two extra TMHs at the interface are attributed to those of CcoH (blue) and cyt *c_y* (red). An additional TMH at the
1162 edge of CIV is attributed to the predicted N-ter TMH of CcoN (TMH0, light purple), and depicted as an *ab initio* model (Methods). **E.**
1163 Enlarged view of CIII₂CIV interface. The view is slightly rotated relative to **A** for better visibility of CcoP TMH in the background (light
1164 blue). Only CcoN TMH9 is shown next to CcoH (blue) and cyt *c_y* (red) TMHs. The fusion region between cyt *c₁* and CcoP is indicated at
1165 the bottom, with the C-ter of cyt *c₁* (green) and the N-ter (resolved portion in the map) of CcoP (light blue) and their respective terminal
1166 residues (Lys257_{*c₁*} and Thr13_{CcoP}). The 12 N-ter CcoP residues connecting these two chains (dashed line) are not clearly resolved. **F.**
1167 Enlarged view showing close interaction between the CcoH and cyt *c_y* TMHs. Characteristic features of cyt *c_y* TMH (NH₂-

1168 **Gly11xxxPhe15xxxxxTyr21**-COOH) are used to determine the registration. The helix break induced by Gly11, and the bulky sidechains
1169 for Phe15 and Tyr21 are clearly visible.

1170

1171

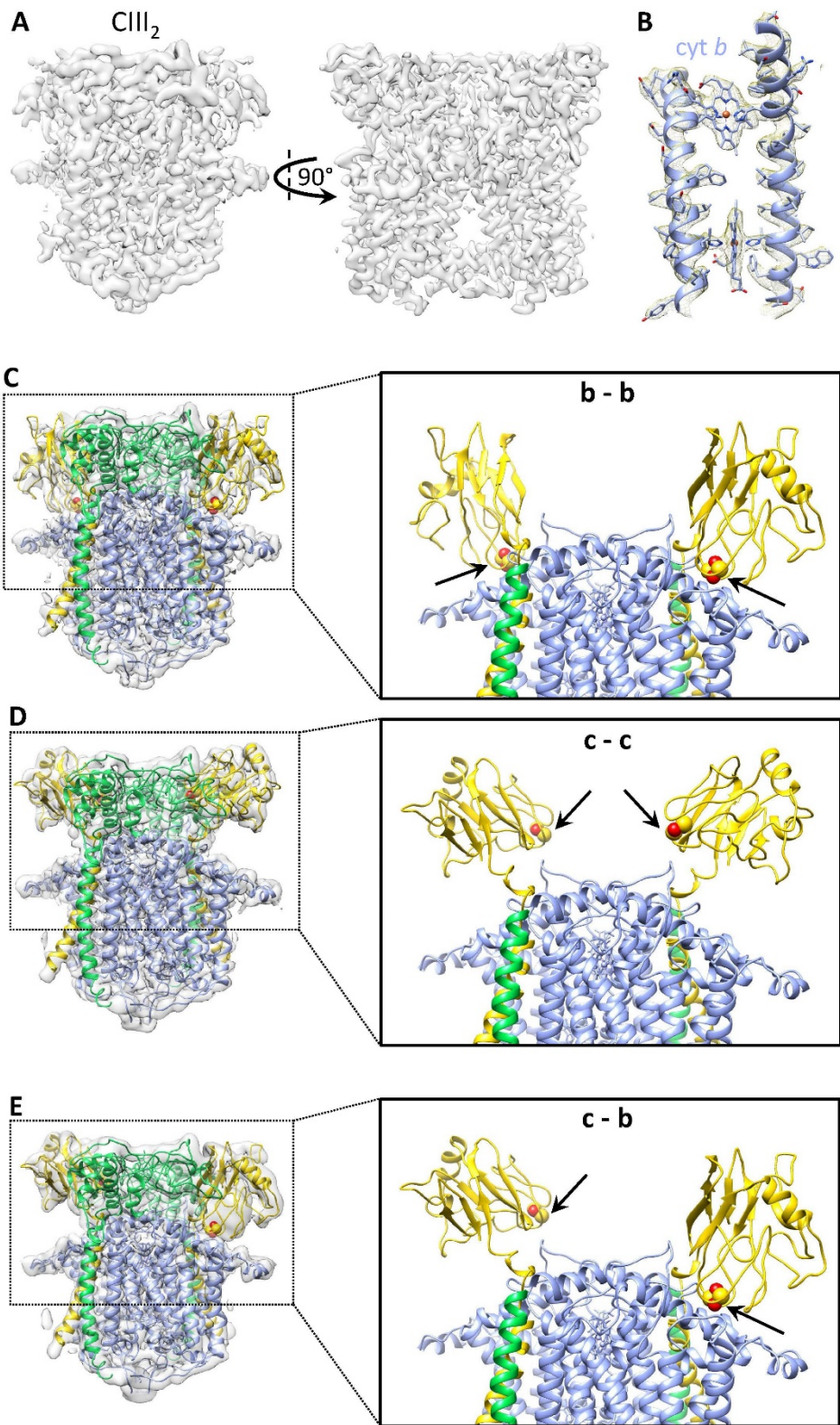


Figure 3. Steimle et al.,

1173 **Figure 3: Structures of native CIII₂ conformers. A.** Cryo-EM map CIII₂ b-b (EMD-22226) with
1174 both FeS proteins in b position. **B.** Representative region of CIII₂ b-b demonstrating map quality and
1175 model fitting. TMH2 and TMH4 of cyt *b* with hemes *b_L* and *b_H* are shown. **C-E.** Maps and models
1176 showing different conformations of the FeS proteins. The left panels show the CIII₂ structure fitted
1177 into the different maps with the subunit colorings (cyt *b* in periwinkle, cyt *c*₁ in green, and the FeS
1178 protein in yellow) as in **Fig. 2**. The right panels show the top half of the models with the membrane-
1179 external domain of cyt *c*₁ omitted to better visualize the b - b, c - c and c - b positions of FeS-EDs.
1180 The [2Fe-2S] clusters are shown as yellow-red spheres and indicated by arrows. **C.** Structure of native
1181 CIII₂ with both FeS-EDs in b position (map CIII₂ b-b, EMD-22226; PDB: 6XKV). **D.** Structure of
1182 native CIII₂ with both FeS-EDs in c position (map CIII₂ c-c, EMD-22224; PDB: 6XKT). and **E.**
1183 Structure of native CIII₂ with one FeS-ED in c and one in b position (map CIII₂ b-c, EMD-22225;
1184 PDB: 6XKU).

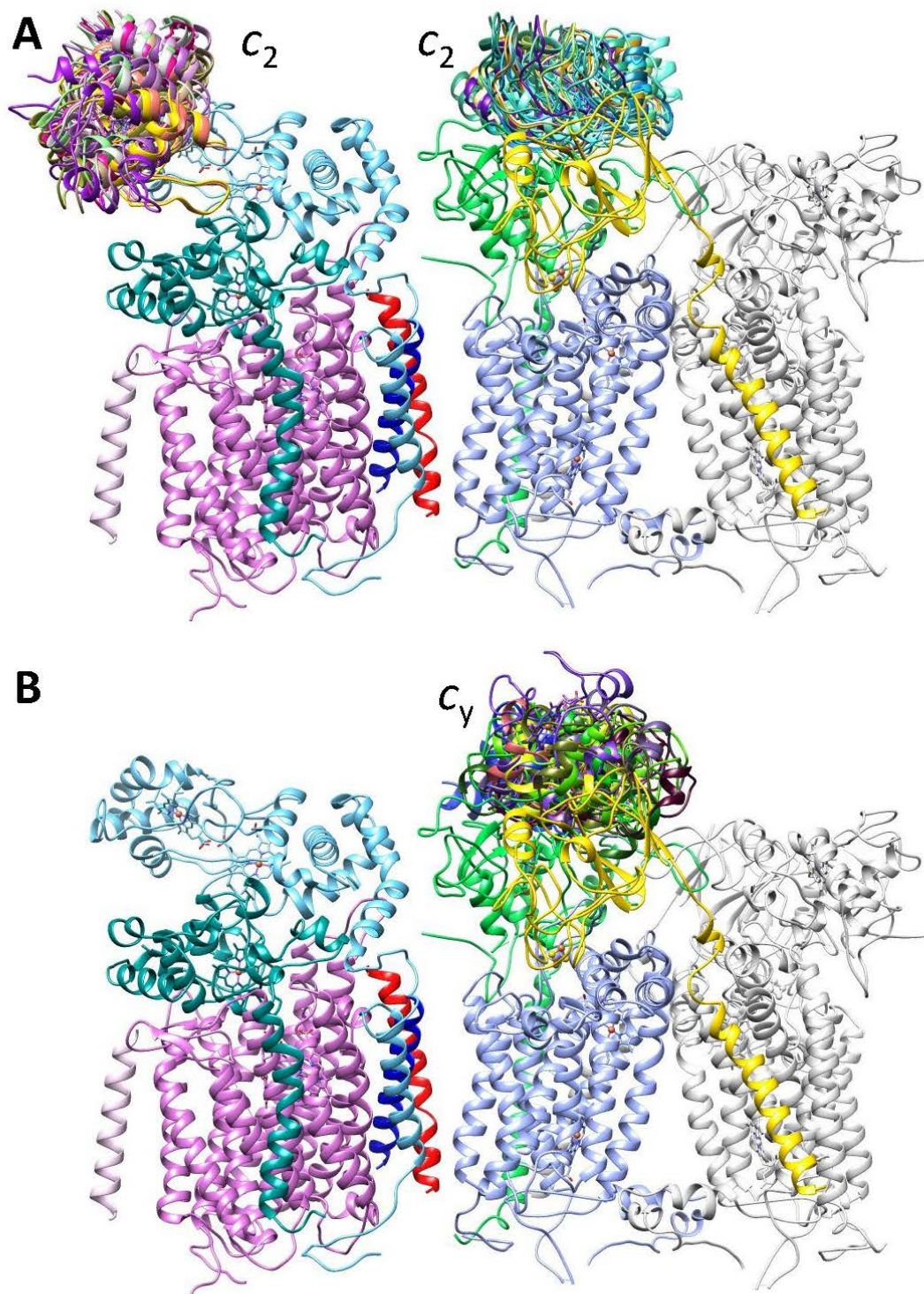


Figure 4. Steimle et al.,

1186 **Figure 4: Binding regions of cyt c_2 and cyt c_y on CIII₂CIV.** The binding regions were defined by
1187 XL-MS guided docking, and the subunits of CIII₂CIV are colored as in **Fig. 2** except the monomer
1188 B of CIII₂ shown in light grey. Only the binding regions on monomer A are shown. **A.** Cyt c_2 (PDB:
1189 1C2N) was docked onto CIII₂ and CIV using Patchdock guided by DMTMM generated XLs as
1190 distance restraints. This yielded one cluster of models on CIV and one per monomer of CIII₂. **B.** A
1191 model of cyt domain of c_y , generated using *P. denitrificans* cyt c_{552} structure (PDB: 3M97) as a
1192 template (RMSD between template and model: 0.2 Å) was docked on CIII₂ as in **A**, except that both
1193 DMTMM and DSBU generated XLs provided distance restraints. Two binding clusters for cyt
1194 domain of c_y per monomer of CIII₂ were found. The two clusters are located behind each other on
1195 a side view, but are clearly visible on top views (**Fig. S4F-H**, labeled 1 and 2). Only cluster 1 which
1196 is closer to cyt c_1 and overlapping with the binding region of cyt c_2 is shown. In all cases, 10
1197 representative models are shown to visualize the clusters of binding models. No binding region for
1198 cyt c_y on CIV could be defined since no XL was found between the proteins.
1199

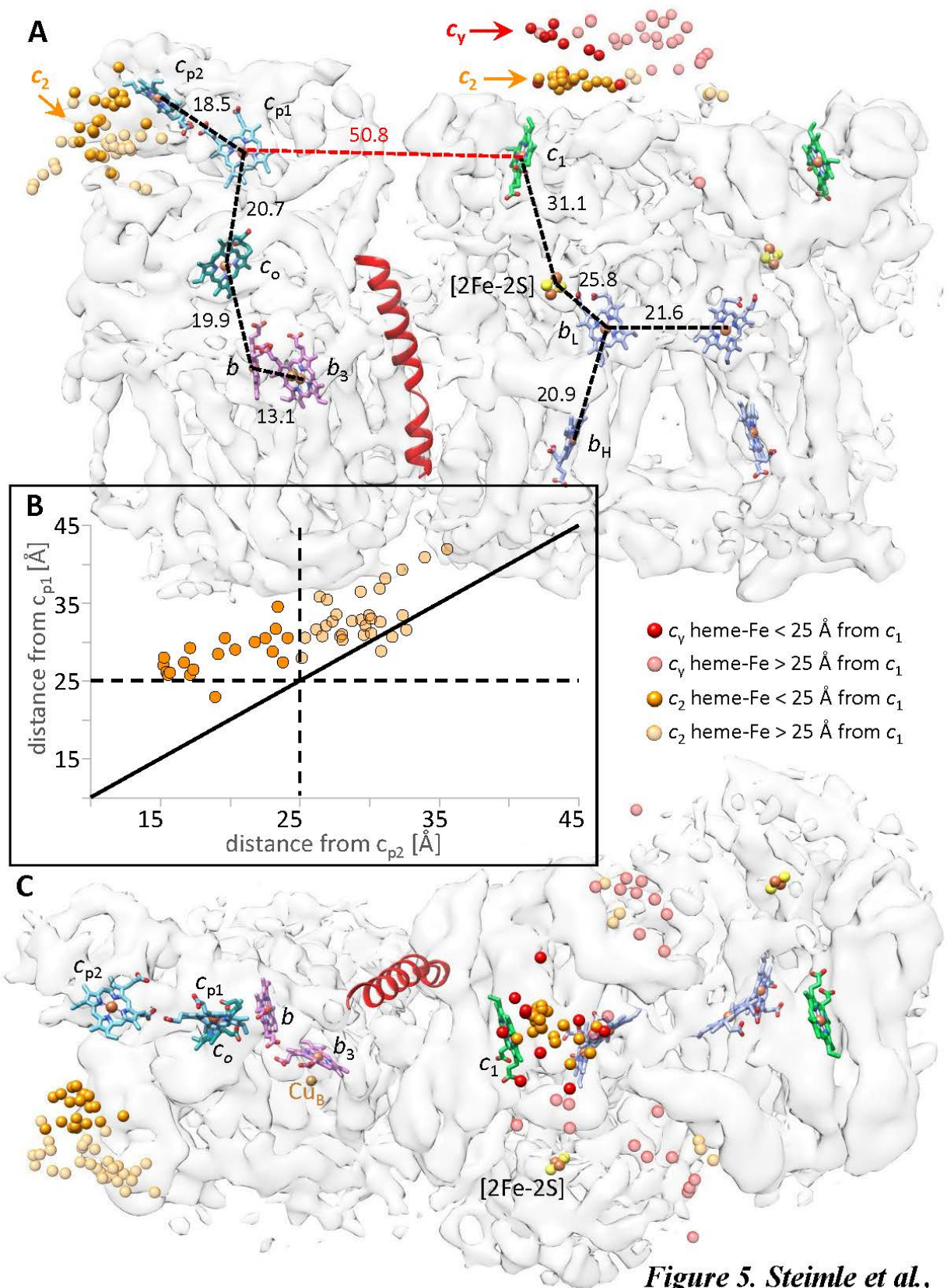


Figure 5. Steimle et al.,

1201 **Figure 5. Organization of CIII₂CIV cofactors and redox partners. A.** The cofactors are shown
1202 inside the transparent map SC-2A of CIII₂CIV with the same subunit colors as in **Fig. 2**: hemes *b_L*
1203 and *b_H* (periwinkle), heme *c₁* (green), hemes *c_{p1}* and *c_{p2}* (light blue), heme *c_o* (dark green), hemes *b*
1204 and *b₃* (purple). The [2Fe-2S] clusters are shown as yellow-red spheres. In all cases the distances
1205 (heme-Fe to heme-Fe) between the heme cofactors are indicated. The positions of docked cyt *c₂* and
1206 cyt domain of *c_y* are indicated as orange (heme *c₂*) and red (heme *c_y*) spheres, respectively,
1207 representing their heme-Fe atoms. All heme-Fe atoms corresponding to the top 50 docking positions
1208 for cyt *c₂* on CIV are shown as solid (< 25Å) or transparent (> 25Å) spheres, depending on their
1209 distances to heme *c_{p2}*. In the case of CIII₂, only the docking positions of cyt *c₂* and cyt *c_y* on monomer
1210 A and between the monomers A and B are shown, omitting those located on monomer B. The TMH
1211 of cyt *c_y* is shown in red at CIII₂CIV interface. **B.** The heme-Fe atoms of all 50 cyt *c₂* models docked
1212 onto CIV are plotted in function of their distances from heme *c_{p1}* and heme *c_{p2}*, with the Fe atoms
1213 within 25Å shown as solid spheres, and those beyond 25Å as transparent spheres. The vast majority
1214 of heme-Fe atoms of docked cyt *c₂* models are closer to heme *c_{p2}* than heme *c_{p1}* of CIV. **C.** Top view
1215 of the map shown in **A** is presented to better visualize the distribution of the docked cyt domain of
1216 *c_y* on monomer A and between the monomers A and B. In all cases, the heme-Fe atoms are depicted
1217 by spheres and colored as indicated above and on the figure.
1218

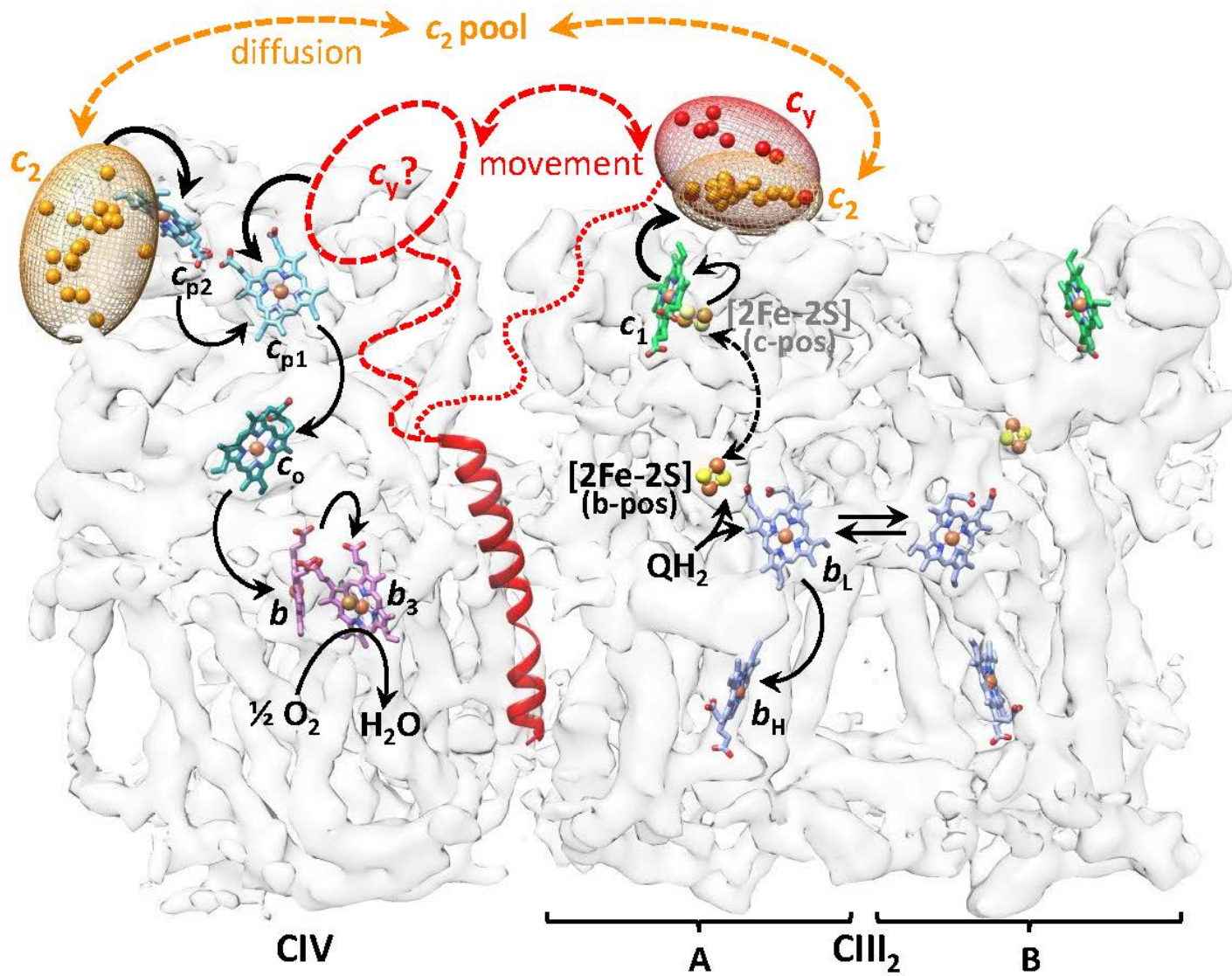


Figure 6. Steimle et al.,

1220 **Figure 6. Proposed cyt c_2 and cyt c_y binding regions of CIII₂CIV and electron transfer pathways.** The likely binding regions of cyt c_2
1221 and cyt c domains of c_y (orange and red ellipsoids, respectively), defined by XL-MS guided docking, are depicted by the distributions of
1222 their heme-Fe atoms on the transparent map SC-2A of CIII₂CIV. Only the positions that are within 25Å of heme c_1 of CIII₂ or heme c_{p2} of
1223 CIV are indicated. The cofactors together with the TMH of cyt c_y are shown as in **Fig. 5**. The linker region (indicated by dotted or dashed
1224 lines) between the TMH and the cyt domain of c_y is not resolved in the cryo-EM map. The proposed electron transport pathways are shown
1225 by thicker black arrows: upon QH₂ oxidation by CIII₂, cyt c_y which is integral to CIII₂CIV receives an electron from heme c_1 . It then moves
1226 (double-headed dashed red arrow) to an undefined binding region (dashed oval with c_y ?) on CIV, where it delivers the electron to the
1227 nearest heme c_{p1} of CIV. Similarly, cyt c_2 which is peripheral to CIII₂CIV also receives an electron from heme c_1 , diffuses away to reach
1228 CIV and conveys it to heme c_{p2} . The canonical electron transfers occurring from QH₂ to heme c_1 in CIII₂, and from heme c_{p1} to O₂ in CIV,
1229 are indicated by thinner arrows. The double headed dashed black arrow depicts the movement of the [2Fe-2S] of FeS protein from the b
1230 position (b-pos, black, solid spheres) to the c position (c-pos, grey, transparent spheres) in CIII₂ during QH₂ oxidation. A possible electron
1231 equilibration between the two heme b_L of CIII₂ is indicated by double arrows, and the electron transfer steps subsequent to heme b_H reduction
1232 are not shown.

Figures

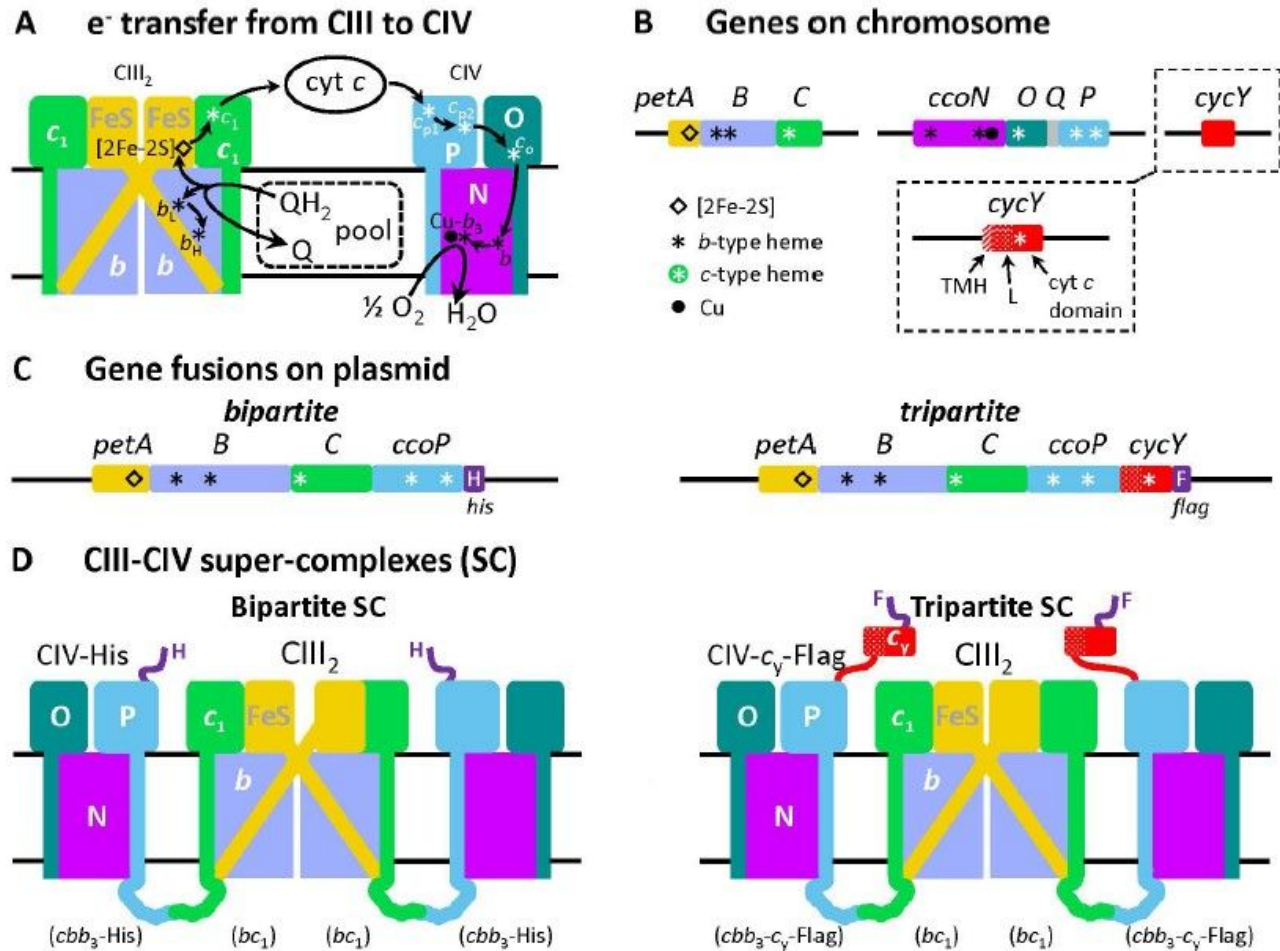


Figure 1

QH₂ oxidation and fused SCs. A. Oxidation of QH₂ to Q by CIII₂ and reduction of O₂ to H₂O by CIV. 1133 A bifurcated electron transfer reaction conveys one electron from QH₂ to the [2Fe-2S] cluster of the FeS protein (FeS, yellow), and another electron to hemes b_L and b_H of cyt b (periwinkle). Reduced [2Fe-2S] cluster transfers the electron to heme c₁ on cyt c₁ (green), via the movement of the FeS protein from near heme b_L to near heme c₁. The subsequent electron transfer step from heme b_H to Q from the pool to form a SQ (semiquinone) is not shown for clarity. A cyt c (c₂ or cy) carries electrons from heme c₁ to CIV, where electrons reach the heme-Cu (Cu b₃) site, where O₂ is reduced to H₂O, via the hemes cp₁ and cp₂ of CcoP (P, light blue), co of CcoO (O, dark green) and heme b of CcoN (N, purple). B. *R. capsulatus* genes used for fused SCs. *petABC* encodes the structural genes of the bc₁-type CIII₂ subunits, the FeS protein (*petA*, yellow), cyt b (B, periwinkle) and cyt c₁ (C, green). *ccoNOQP* encodes the structural genes of the cbb₃-type CIV subunits, the CcoN (*ccoN*, purple), CcoO (O, dark green), CcoQ (Q, grey) and CcoP (P, light blue). *cycY* gene (red) encodes the membrane-anchored cyt cy, and its 30-residue transmembrane helix (TMH), 69-residue linker (L) and 100-residue cyt c (cyt c) domain are indicated. Heme cofactors of b- and

c-type cyts are indicated by black and white asterisks, respectively, whereas diamond and dot designate the [2Fe-2S] cluster and Cu atom, respectively. C. Plasmid-borne genetic fusions. The bipartite fusion (left) is formed by in-frame linking the 3'-end of *petC* to the 5'-end of *ccoP*, and the tripartite fusion (right) by adding the linker and *cyt c* domain of *cycY* to the 3'-end of *ccoP*. Colors and cofactor symbols are as in A, and the His (H) and Flag (F) affinity tags (dark purple) at the 3'-end of the bipartite and tripartite fusion subunits are shown. D. Schematic depiction of bipartite (left) and tripartite (right) super-complexes (SC). The bipartite SC encodes a CIII₂ dimer fused on each side to a His-tagged CIV. The tripartite SC also contains the Flag-tagged *cyt c* domain of *cy* (red) at the end of *CcoP* (blue).

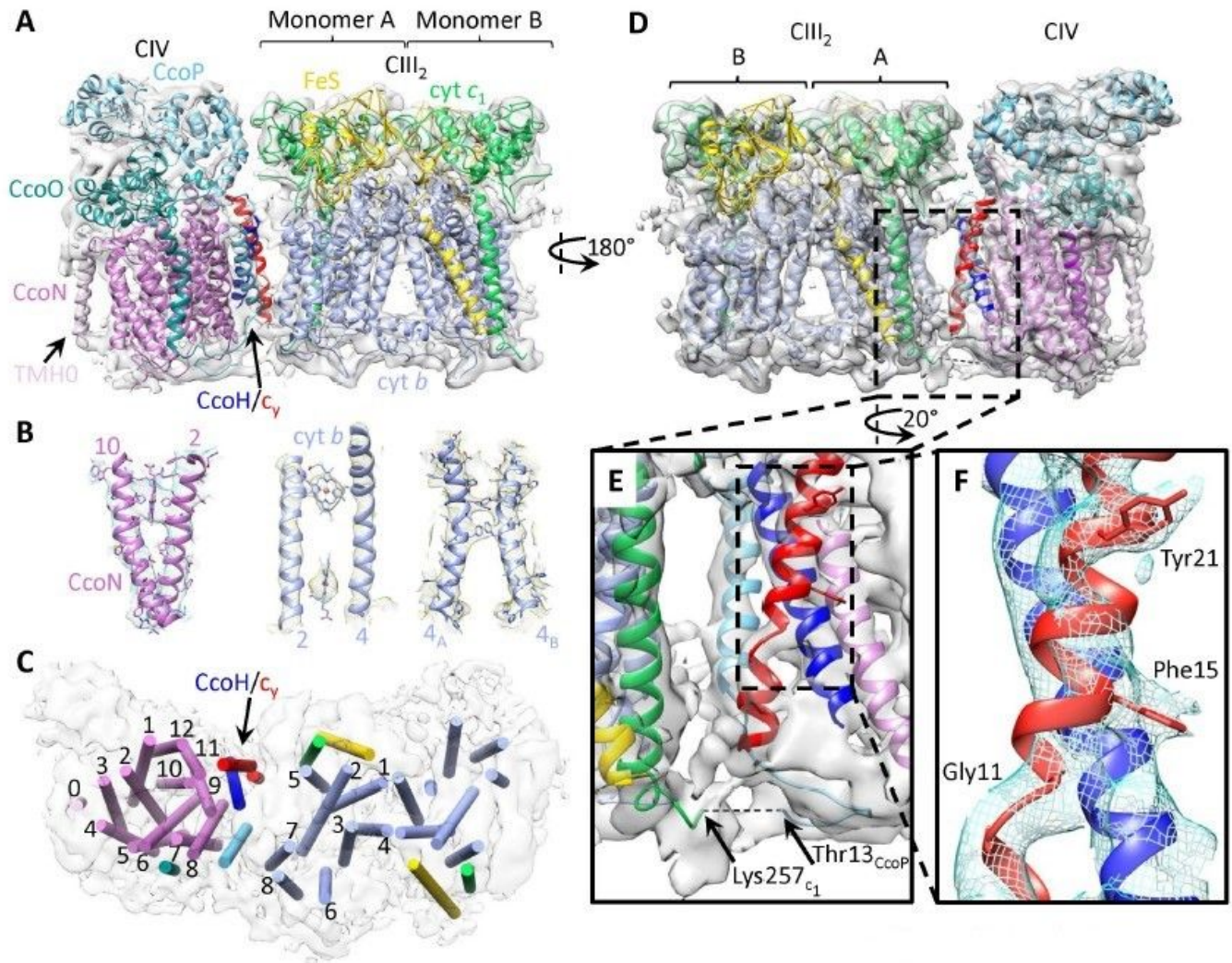


Figure 2

Cryo-EM structure of CIII₂CIV. A. Side view of CIII₂CIV. The structures of CIII₂ (PDB: 6XI0), 1151 and the homology model of *R. capsulatus* *cbb3*-type CIV were fitted into the cryo-EM map SC-2A depicted in transparent grey. All subunits are colored and labelled as indicated, and the additional feature indicated by an arrow at the edge of CcoN subunit of CIV corresponds to the extra N-ter TMH (TMH0, light purple) specific to *R. capsulatus*. The large arrow points out the CcoH/*cy* helices in red/blue. B. Representative

regions of the cryo-EM map showing the map quality and model fitting. The TMH2 and TMH10 of CcoN (left) show clearly heme b and some bulky side chains. Only the protein backbone and hemes bL and bH are resolved between the TMH2 and TMH4 of cyt b (center) (see Fig. 3B for comparison with CIII2 map at 3.3 Å). Large side chains are clearly visible between the TMH4 of monomer A and TMH4 of monomer B of CIII2 (4A and 4B, respectively; right). C. Top view of CIII2CIV with TMHs depicted as cylinders and colored as in A. The TMHs of cyt b (only CIII2 monomer A) and CcoN of CIV are numbered, and the TMHs of the FeS protein (yellow), cyt c1 (green), CcoO (dark green), CcoP (light blue), CcoH/cy (blue/red with an arrow) and CcoN TMH0 (light purple) are shown. D. 180° rotated view for the back view of CIII2CIV interface. The two extra TMHs at the interface are attributed to those of CcoH (blue) and cyt cy (red). An additional TMH at the edge of CIV is attributed to the predicted N-ter TMH of CcoN (TMH0, light purple), and depicted as an ab initio model (Methods). E. Enlarged view of CIII2CIV interface. The view is slightly rotated relative to A for better visibility of CcoP TMH in the background (light blue). Only CcoN TMH9 is shown next to CcoH (blue) and cyt cy (red) TMHs. The fusion region between cyt c1 and CcoP is indicated at the bottom, with the C-ter of cyt c1 (green) and the N-ter (resolved portion in the map) of CcoP (light blue) and their respective terminal residues (Lys257c1 and Thr13CcoP). The 12 N-ter CcoP residues connecting these two chains (dashed line) are not clearly resolved. F. Enlarged view showing close interaction between the CcoH and cyt cy TMHs. Characteristic features of cyt cy TMH (NH2-51 Gly11xxxPhe15xxxxxTyr21-COOH) are used to determine the registration. The helix break induced by Gly11, and the bulky sidechains for Phe15 and Tyr21 are clearly visible.

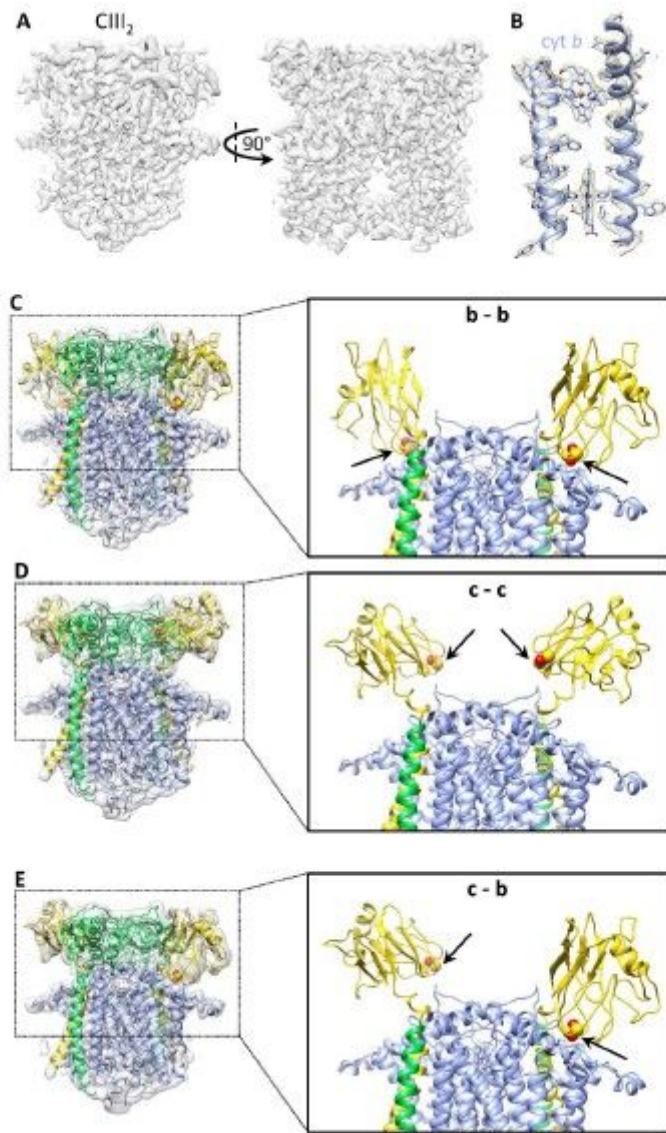


Figure 3

Structures of native CIII2 conformers. A. Cryo-EM map 1173 CIII2 b-b (EMD-22226) with both FeS proteins in b position. B. Representative region of CIII2 b-b demonstrating map quality and model fitting. TMH2 and TMH4 of cyt b with hemes bL and bH are shown. C-E. Maps and models showing different conformations of the FeS proteins. The left panels show the CIII2 structure fitted into the different maps with the subunit colorings (cyt b in periwinkle, cyt c1 in green, and the FeS protein in yellow) as in Fig. 2. The right panels show the top half of the models with the membrane external domain of cyt c1 omitted to better visualize the b - b, c - c and c - b positions of FeS-EDs. The [2Fe-2S] clusters are shown as yellow-red spheres and indicated by arrows. C. Structure of native CIII2 with both FeS-EDs in b position (map CIII2 b-b, EMD-22226; PDB: 6XKV). D. Structure of native CIII2 with both FeS-EDs in c position (map CIII2 c-c, EMD-22224; PDB: 6XKT). and E. Structure of native CIII2 with one FeS-ED in c and one in b position (map CIII2 b-c, EMD-22225; PDB: 6XKU).

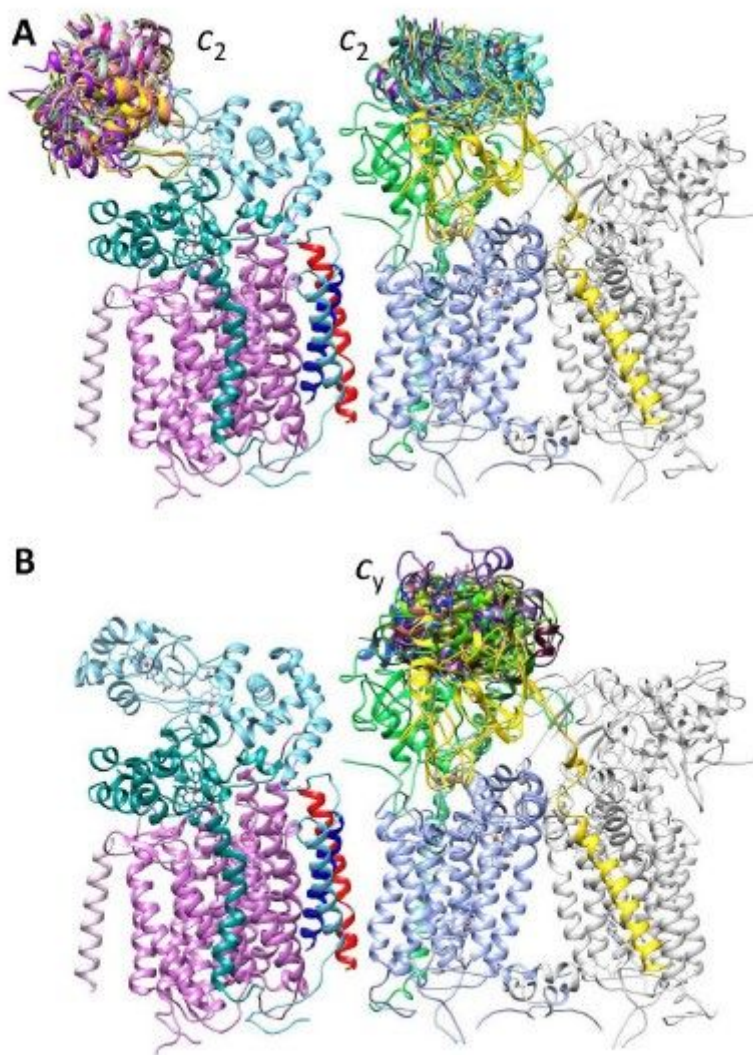


Figure 4

Binding regions of cyt c2 and cyt cy on CIII2CIV. The binding 1186 regions were defined by XL-MS guided docking, and the subunits of CIII2CIV are colored as in Fig. 2 except the monomer B of CIII2 shown in light grey. Only the binding regions on monomer A are shown. A. Cyt c2 (PDB: 1C2N) was docked onto CIII2 and CIV using Patchdock guided by DMTMM generated XLs as distance restraints. This yielded one cluster of models on CIV and one per monomer of CIII2. B. A model of cyt domain of cy, generated using *P. denitrificans* cyt c552 structure (PDB: 3M97) as a template (RMSD between template and model: 0.2 Å) was docked on CIII2 as in A, except that both DMTMM and DSBU generated XLs provided distance restraints. Two binding clusters for cytochrome cy per monomer of CIII2 were found. The two clusters are located behind each other on a side view, but are clearly visible on top views (Fig. S4F-H, labeled 1 and 2). Only cluster 1 which is closer to cyt c1 and overlapping with the binding region of cyt c2 is shown. In all cases, 10 representative models are shown to visualize the clusters of binding models. No binding region for cyt cy on CIV could be defined since no XL was found between the proteins.

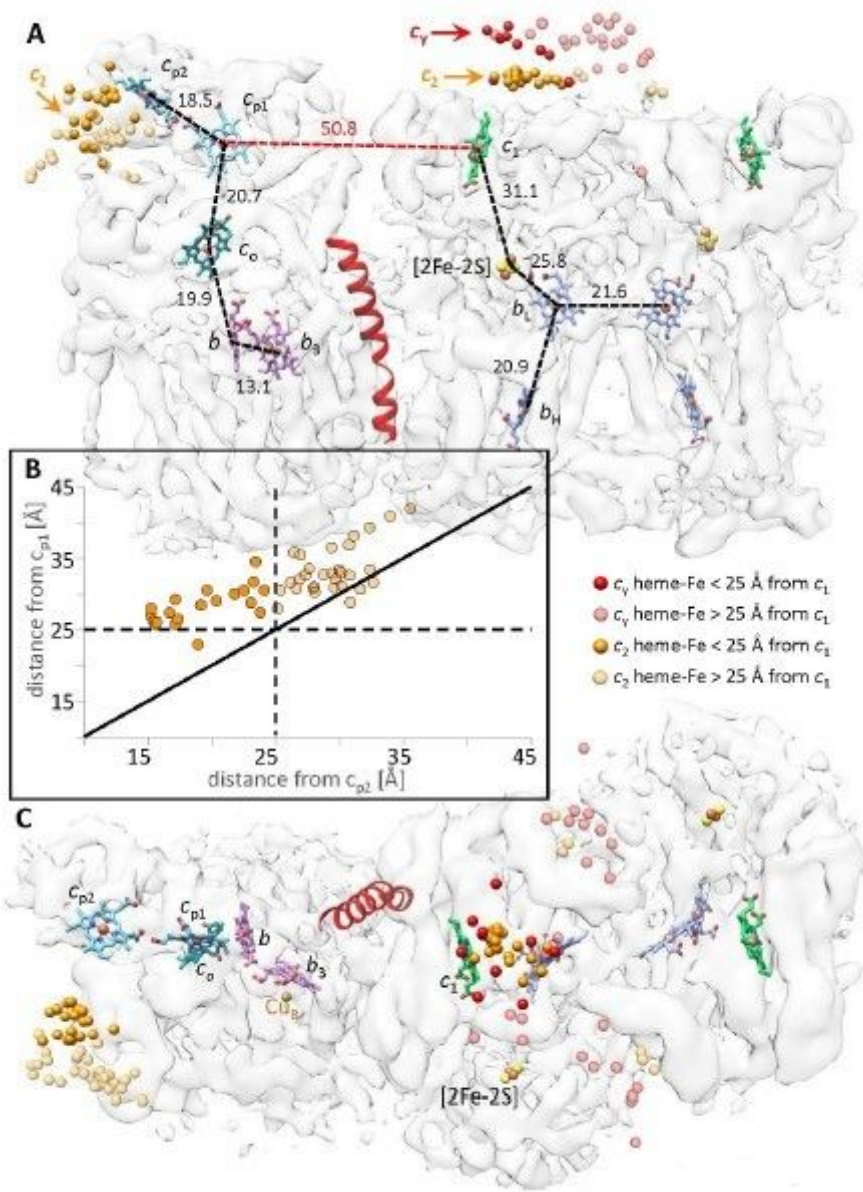


Figure 5

Organization of CIII2CIV cofactors and redox partners. A. The 1201 cofactors are shown inside the transparent map SC-2A of CIII2CIV with the same subunit colors as in Fig. 2: hemes bL and bH (periwinkle), heme c1 (green), hemes cp1 and cp2 (light blue), heme co (dark green), hemes b and b3 (purple). The [2Fe-2S] clusters are shown as yellow-red spheres. In all cases the distances (heme-Fe to heme-Fe) between the heme cofactors are indicated. The positions of docked cyt c2 and cyt domain of cy are indicated as orange (heme c2) and red (heme cy) spheres, respectively, representing their heme-Fe atoms. All heme-Fe atoms corresponding to the top 50 docking positions for cyt c2 on CIV are shown as solid (< 25Å) or transparent (> 25Å) spheres, depending on their distances to heme cp2. In the case of CIII2, only the docking positions of cyt c2 and cyt cy on monomer A and between the monomers A and B are shown, omitting those located on monomer B. The TMH of cyt cy is shown in red at CIII2CIV interface. B. The heme-Fe atoms of all 50 cyt c2 models docked onto CIV are plotted in function of their distances

from heme cp1 and heme cp2, with the Fe atoms within 25Å shown as solid spheres, and those beyond 25Å as transparent spheres. The vast majority of heme-Fe atoms of docked cyt c2 models are closer to heme cp2 than heme cp1 of CIV. C. Top view of the map shown in A is presented to better visualize the distribution of the docked cyt domain of cy on monomer A and between the monomers A and B. In all cases, the heme-Fe atoms are depicted by spheres and colored as indicated above and on the figure.

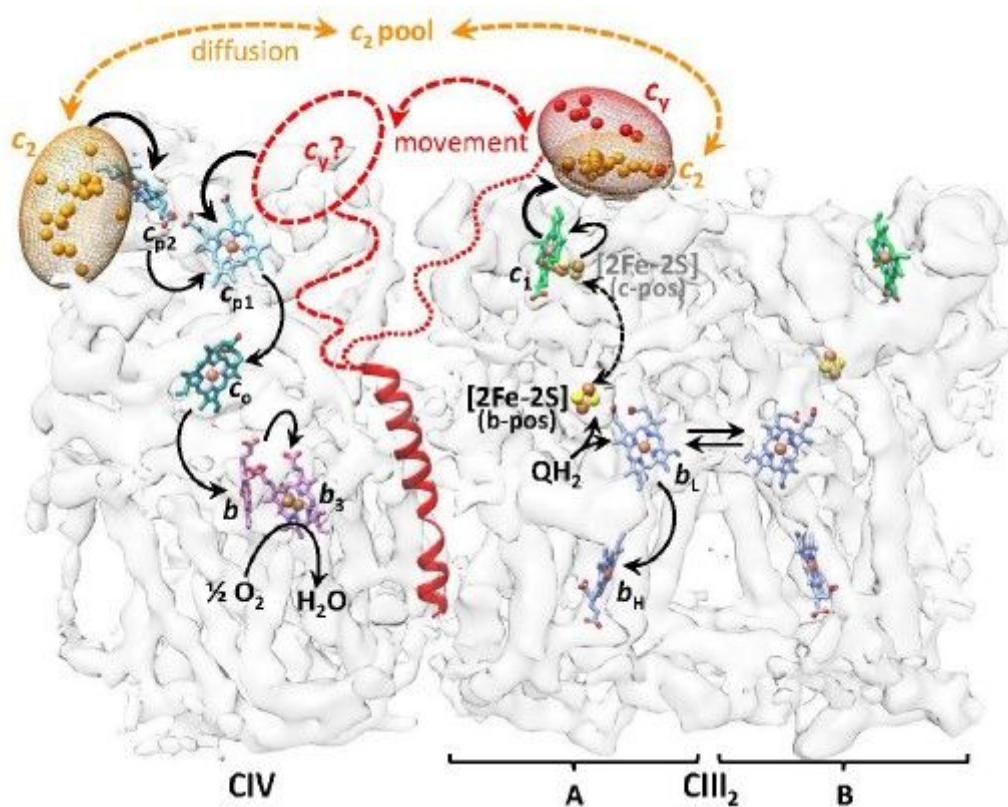


Figure 6

Proposed cytochrome c2 and cytochrome cy binding regions of CIII2CIV and electron transfer pathways. The likely 1220 binding regions of cytochrome c2 and cytochrome c domains of cy (orange and red ellipsoids, respectively), defined by XL-MS guided docking, are depicted by the distributions of their heme-Fe atoms on the transparent map SC-2A of CIII2CIV. Only the positions that are within 25Å of heme c1 of CIII2 or heme cp2 of CIV are indicated. The cofactors together with the TMH of cytochrome cy are shown as in Fig. 5. The linker region (indicated by dotted or dashed lines) between the TMH and the cytochrome domain of cy is not resolved in the cryo-EM map. The proposed electron transport pathways are shown by thicker black arrows: upon QH2 oxidation by CIII2, cytochrome cy which is integral to CIII2CIV receives an electron from heme c1. It then moves (double-headed dashed red arrow) to an undefined binding region (dashed oval with cy?) on CIV, where it delivers the electron to the nearest heme cp1 of CIV. Similarly, cytochrome c2 which is peripheral to CIII2CIV also receives an electron from heme c1, diffuses away to reach CIV and conveys it to heme cp2. The canonical electron transfers occurring from QH2 to heme c1 in CIII2, and from heme cp1 to O2 in CIV, are indicated by thinner arrows. The double headed dashed black arrow depicts the movement of the [2Fe-2S] of FeS protein from the b position (b-pos, black, solid spheres) to the c position (c-pos, grey, transparent spheres) in CIII2

during QH2 oxidation. A possible electron equilibration between the two heme bL of CIII2 is indicated by double arrows, and the electron transfer steps subsequent to heme bH reduction are not shown.

Supplementary Files

This is a list of supplementary files associated with this preprint. Click to download.

- [SCSupplementfiguresinserted.pdf](#)
- [nrreportingsummaryDaldal.pdf](#)
- [validationreportsDaldal.zip](#)